Analysis of the flexural response of hybrid reinforced concrete beams with localized reinforcement corrosion

(article starts on next page)

ARTICLE

Analysis of the flexural response of hybrid reinforced concrete beams with localized reinforcement corrosion

Carlos G. Berrocal[1,2] | E Chen[3] | Ingemar Löfgren[1,2] | Karin Lundgren[1]

[1]Structural Engineering Division, Chalmers University of Technology, Gothenburg, Sweden

[2]Thomas Concrete Group C-lab, Gothenburg, Sweden

[3]School of Civil and Hydraulic Engineering, Huazhong University of Science and Technology, Wuhan, China

Correspondence
Carlos G. Berrocal, Structural Engineering Division, Chalmers University of Technology, Gothenburg, Sweden.
Email: carlos.gil@chalmers.se

Abstract

This paper presents a modeling approach to analyze the flexural response of hybrid reinforced concrete beams with localized corrosion. A new mechanical model based on extensive uniaxial testing is proposed to describe the stress–strain relationship of corroded bars with a single pit. The proposed mechanical model is then incorporated into a sectional analysis to determine the moment curvature relationship of hybrid reinforced concrete sections with pitting corrosion. The actual crack pattern is used to divide a beam into discrete hinge elements which are then combined to compute the load–deflection response of statically determinate beams. The modeling approach is evaluated with available experimental data showing good predictive capabilities. A parametric study revealed the importance of the interaction between the tensile reinforcement ratio and the concrete postcracking residual stress. Furthermore, the deformation capacity of reinforcement bars with pitting corrosion levels beyond 0.25 was shown to have a dominant effect on the ultimate deflection of hybrid reinforced concrete beams.

KEYWORDS
deformation capacity, flexural resposnse, hinge model, hybrid reinforced concrete, pitting corrosion, strain localization

1 | INTRODUCTION

Corrosion of reinforcement is the main degradation process affecting the durability and safety of reinforced concrete (RC) structures worldwide. Among the consequences of reinforcement corrosion, localized pitting has been found particularly detrimental as the deformation capacity of the reinforcement is rapidly decreased due to strain localization at the pits.[1–3] As such, corrosion has a severe negative impact on the structural performance of corroded structures which in turn may compromise the safety of the users.

It is generally accepted that too large cracks lead to premature corrosion initiation. As a result, the use of fiber reinforced concrete (FRC) in combination with traditional rebar, also referred to as hybrid reinforced concrete (hybrid-RC), leads to a reduced crack spacing and lower stresses in the rebar, resulting in smaller crack widths compared to traditional RC.[4–9] Additional reported benefits of hybrid-RC include a slower ingress of external agents due to multiple internal microcracks,[10] delayed corrosion

initiation,[11,12] an enhanced residual bond[13,14] as well as the suppression of corrosion-induced spalling.[13,15] Moreover, the greater corrosion resistance of steel fibers compared to conventional rebar[16,17] results in a slower degradation of the load capacity in hybrid-RC elements, as experimentally observed for beams containing a moderate steel fiber content (<1% vol.).[18] Furthermore, hybrid-RC has also been recently shown to be a more sustainable solution for crack control than RC from a life cycle perspective.[19] Despite the positive effects of hybrid-RC, to completely suppress corrosion is a challenging pursuit. To that end, developing tools and models to estimate the residual structural behavior of corroding RC members is crucial.

In the past, several studies have outlined different strategies to analyze the residual behavior of corroded RC structures, most of which were based on finite element (FE) analyses. For instance, Jnaid and Aboutaha[20] used finite FE analyses where the yield strength of the corroded reinforcement was reduced proportionally to the corrosion level and complete loss of bond was assumed for corroded bar regions. Similarly, Lee et al.[21] used FE analyses with modified yield strength, elastic modulus and bond properties of the reinforcement where the proposed relationships were expressed as a linear function of the average corrosion level with different scaling factors for uniform and pitting corrosion. Lim et al.[22] investigated the effect of the spatial variability of reinforcement corrosion on the structural behavior of RC beams. In their approach, the local variation of corrosion along the reinforcement was explicitly considered in the FE models and a bilinear stress–strain relationship, scaled by the local corrosion level, was used to describe the mechanical properties of the corroded reinforcement. In a recent study by Habibi et al.[23] FE analyses were also adopted to investigate the flexural response of corroded RC members but including an explicit reduction of the ultimate strain of the corroded bars expressed as a linear function of the corrosion level. In the work by Nasser et al.,[24] FE analyses were carried out where specific consideration was given to the deformation capacity of the bar taking into account the pit length and the uncorroded bar length. Similarly, Haefliger and Kaufmann,[25] extended an existing model to include the effects of corrosion, where the effect of strain localization due to pitting and the concept of critical corrosion level were introduced while steel reinforcement was modeled using a nonlinear stress–strain law including the yielding plateau and strain hardening.

Due to the strong influence that the position of transverse cracks has on the formation of corrosion pits,[26,27] it has been observed that hybrid-RC elements present a greater number of corrosion pits but with a lower corrosion level than for traditional RC elements.[27] However, it is unclear whether and how different corrosion pit distributions, including the number of pits, their location, the distribution of local corrosion and the position along the rebar of the most severe pit, could influence the flexural behavior of hybrid-RC elements. Therefore, a model that can conveniently incorporate the position of preexisting cracks and the corrosion distribution along the member would be useful. To the authors' knowledge, no model (empirical or theoretical) has yet been proposed to study the residual flexural behavior of hybrid-RC elements with corroding reinforcement.

The nonlinear hinge model, initially proposed by Ulfkjaer et al.,[28] was developed to study the sectional behavior of FRC beams. The original idea of the nonlinear hinge model is that the flexural behavior of a beam can be approximated by describing the cracked section as a nonlinear hinge and assuming that the rest of the structure behaves elastically. The description of the crack propagation in concrete is based on nonlinear fracture mechanics through the "fictitious crack model" as suggested by Hillerborg for plain concrete[29] and FRC.[30] The nonlinear hinge model is well suited to describe unreinforced concrete or FRC concrete sections with tension softening behavior where a single crack develops and it has been used by several researchers to study the flexural behavior of FRC beams.[31–33] In later work by Olesen,[34] the nonlinear hinge model was extended to analyze the sectional behavior (moment–curvature) of hybrid-RC elements including the variation of stresses along the reinforcement due to bond action. In that work, the length of the nonlinear hinge, which had been initially suggested to be half of the beam depth, was assumed as the length of debonded reinforcement on each side of the crack. However, since the debonded length is a function of the load, the length of the hinge must adapt over the analysis, hence the approach was named the adaptive hinge element.

In this work, a model to analyze the global flexural behavior (force–deflection) of hybrid-RC beams with localized corrosion is proposed. The approach adopted is to discretize a beam into a series of nonlinear hinges based on available information about the position of preexisting transverse cracks. Subsequently, the sectional behavior of each hinge is analyzed, where the effect of discrete pits on the stress–strain relationship of corroding rebar is considered based on previous work by the authors.[35] In the following sections, the model is described and evaluated against different experimental results including both RC and hybrid-RC, with and without corrosion. Subsequently, a parametric study is carried out to investigate the influence of several aspects, including the maximum corrosion level, the postcracking behavior of FRC and the corrosion distribution, on the load and deformation capacity.
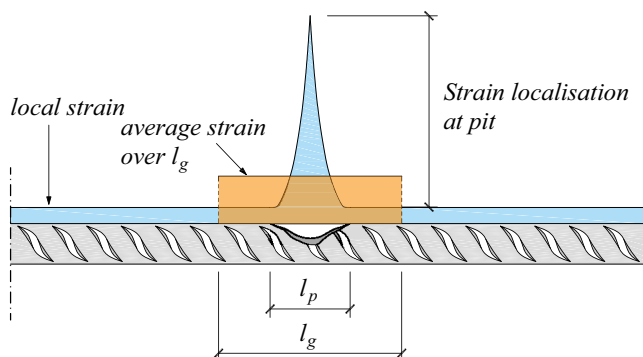
FIGURE 1 Schematic representation of the distribution of local strain along a bar with a pit of length l_p and the engineering strain over the pit measured with a gauge length of l_g. Note that the local effect of the ribs has not been included.

2 | MODELING STEEL REINFORCEMENT WITH LOCALIZED CORROSION

2.1 | Effect of corrosion on steel reinforcement

When corrosion occurs simultaneously along a large surface area of a reinforcing bar, it is often referred to as general or uniform corrosion. This type of corrosion is usually ascribed to a generalized reduction of the pH in the concrete pore solution due to carbonation. In quenched and self-tempered (QST) steel reinforcing bars, often referred to as TempCore® bars, uniform corrosion can have a severe effect on the strength. This is due to the heterogeneous microstructure of the material which consists of a high-strength outer-martensitic tempered ring and a ductile ferritic–perlitic inner core.[36] However, due to the volumetric expansion of the corrosion products, uniform corrosion can often be detected early in the degradation process due to the formation of longitudinal cracking and the appearance of conspicuous rust stains on the concrete surface.

On the other hand, localized corrosion, also referred to as pitting corrosion, describes a type of corrosion characterized by the formation of a corrosion macrocell that leads to a rapid and highly localized loss of cross-sectional area. Pitting corrosion occurs as a result of the local breakdown of the steel passive layer due to the presence of chlorides and, unlike for uniform corrosion, cover cracking might be delayed, thereby concealing the actual condition of the reinforcement and making corrosion harder to detect. The local loss of cross-section in a QST reinforcing bar does not significantly affect the apparent strength of the material as both the outer ring and the inner core are often affected. However, it has been experimentally observed[35,37,38] that localized pitting strongly reduces the deformation capacity of reinforcing bars due to strain localization. This effect is illustrated in Figure 1, where the difference between the local strain at each section of the bar and the engineering strain measured over a gauge length, l_g, that includes a pit of length, l_p, is highlighted. Since engineering strain is always linked to a certain reference gauge length, the steel strain is denoted and defined as:

$$\varepsilon_s^{l_g} = \frac{\Delta L}{l_g} \tag{1}$$

where ΔL is the length change of the measuring device, for example, an extensometer, and l_g is the reference gauge length.

In a recent study by Franceschini et al.,[39] a stress–strain relationship for prestressing steel strands with localized pitting corrosion was derived based on 3D scanning data of naturally corroded strands where the maximum penetration depth of the pit was used as main parameter. In this work, a similar approach was adopted where experimental results from a previous study[35] were analyzed to derive the parameters required to define the engineering stress–strain relationship of steel reinforcement bars with localized corrosion, although as a function of the maximum corrosion level in a pit, μ, defined as:

$$\mu = \frac{A_s - A_{pit}}{A_s} \tag{2}$$

where A_s and A_{pit} are the uncorroded cross-sectional area of the bar and the minimum residual cross-sectional area at the pit, respectively.

In Chen et al.,[35] the mechanical behavior of more than 50 TempCore® B500B steel reinforcement bars with a single major pit of varying corrosion levels was obtained experimentally through uniaxial tensile tests. Before the tensile tests, a 3D laser scanner was used to determine the residual cross-section area of the corroded bars, A_{pit} with high accuracy. In the uniaxial tests, an extensometer with a gauge length of 50 mm was used to measure the average strain. Henceforth, when a superscript is not specified, strain will be referred to a 50 mm gauge length, that is, $\varepsilon_s = \varepsilon_s^{50}$.

The force–strain diagram for all the tested bars with maximum corrosion levels between 0 and 0.337 is presented in Figure 2a. As observed, uncorroded rebars displayed a behavior that can be described by four different stages: (i) elastic stage, (ii) yield plateau, (iii) hardening stage, and (iv) necking or softening stage. The schematic representation of the stress strain diagram for an uncorroded bar is shown in Figure 2b, where the characteristic
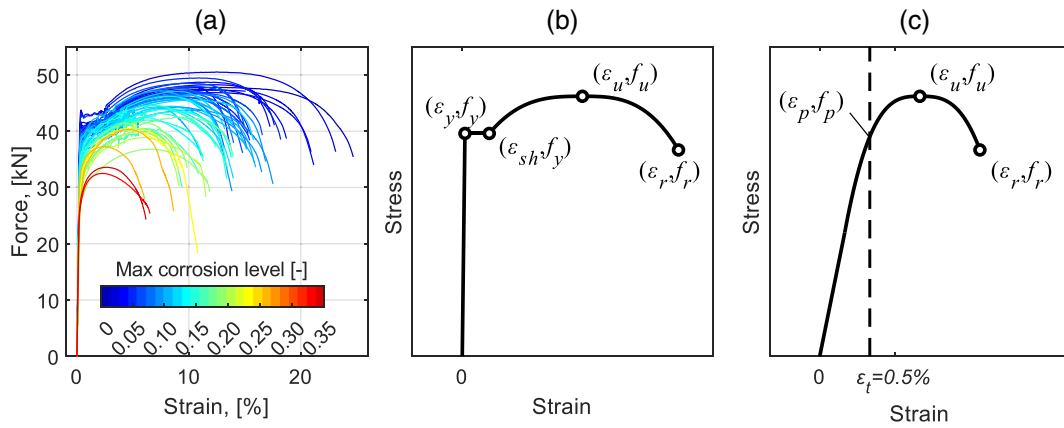
FIGURE 2 (a) Experimental results of force–strain diagram for 53 reinforcing bars with varying maximum corrosion levels, after.[35] Schematic representation of the stress–strain diagram of TempCore® reinforcement bars for (b) uncorroded rebar and (c) rebar with significant corrosion. The subscripts in (b) and (c) stand for yield "y," strain hardening "sh," ultimate "u," rupture "r," and proof "p."
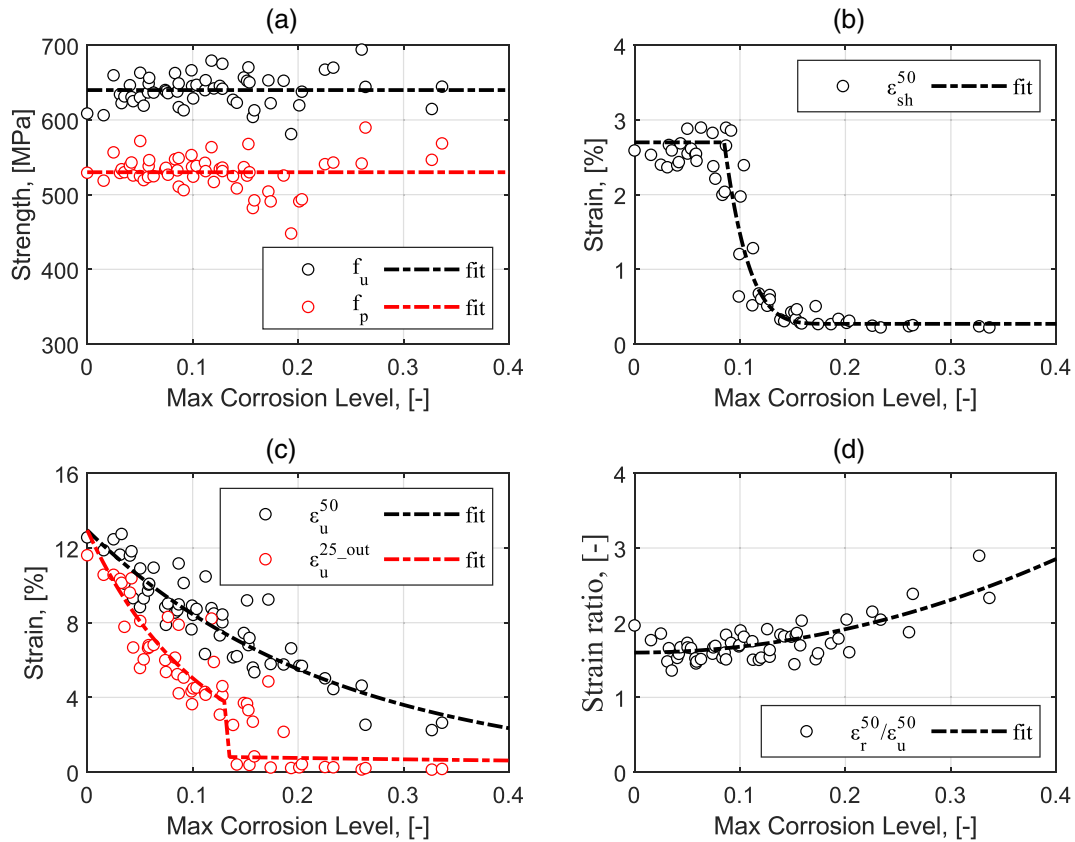
FIGURE 3 Variation of parameters describing the mechanical behavior of steel reinforcement bars with increasing localized corrosion level: (a) ultimate and proof strength; (b) strain at the onset of steel hardening; (c) ultimate strain across the pit measured with a 50 mm extensometer and ultimate strain outside the pit measured with a 25 mm extensometer; and (d) ratio between the strain at rupture and the ultimate strain across the pit.

points defining the boundaries of the different stages of the diagram have been identified.

According to previous findings, in addition to a decrease of the load capacity, reinforcement bars with localized corrosion exhibited a sharp reduction of their deformation capacity. Moreover, the shape of the diagram was also affected, and the yield plateau became less and less obvious with increasing corrosion levels, until it was no longer discernible. For steel without a yield plateau, such as cold formed steel, the concept of yield strength is usually replaced by proof strength, which is defined as the stress at a prescribed plastic or total strain.[40] Consequently,

since the pronounced effect of corrosion on the force–strain diagram made it difficult to accurately determine the force and stress at yielding, a proof strain of 0.5% (measured also by an extensometer with a gauge length of 50 mm) was used in this study to analyze the mechanical behavior of heavily corroded rebars. It should be noted that for uncorroded bars and lightly corroded bars exhibiting the yield plateau, the proof strength at 0.5% strain is virtually the same as the yield strength. The schematic representation of the stress strain diagram for a bar with significant localized corrosion is presented in Figure 2c.

In Figure 3, the variation with the maximum corrosion at the pit of some of the characteristic points shown in Figure 2b,c is presented. Figure 3a shows the proof strength, f_p, and ultimate strength, f_u, calculated as:

$$f_p = \frac{F_p}{A_s(1-\mu)} \tag{3}$$

$$f_u = \frac{F_u}{A_s(1-\mu)} \tag{4}$$

where F_p and F_u are the proof and ultimate force of the bar, respectively.

As observed, neither the ultimate nor the proof strength appeared to depend on the corrosion level; they were both scattered around a value close to the one measured for uncorroded bars. Consequently, both strengths were assumed independent of the corrosion level at the pit and were taken as the average value of the measured points, namely $f_p = 530$ MPa and $f_u = 640$ MPa.

The variation of the strain at the onset of strain hardening with increasing corrosion is shown in Figure 3b. It can be seen that for lightly corroded bars with a maximum corrosion level below approximately 0.085, the value is also scattered around the initial value of the strain at the onset of hardening, $\varepsilon_{sh,0} = 0.027$. However, beyond a corrosion level of 0.085, an abrupt drop occurs which seems to stabilize at a value equal to the initial yield strain $\varepsilon_{y,0} = 0.0027$ for corrosion levels greater than 0.2. This means that for corrosion levels beyond 0.2 the yield plateau is no longer discernible, although the observed trend still needs to be verified for very large corrosion levels, that is, $\mu > 0.5$. The strain at the onset of strain hardening as a function of the corrosion level is defined as:

$$\varepsilon_{sh}(\mu) = \begin{cases} \varepsilon_{sh,0} & \mu < 0.085 \\ \varepsilon_{y,0} + \left(\varepsilon_{sh,0} - \varepsilon_{y,0}\right)\left(\frac{0.2 - \mu}{0.2 - 0.085}\right)^{\alpha_h} & 0.085 < \mu < 0.2 \\ \varepsilon_{y,0} & \mu > 0.2 \end{cases} \tag{5}$$

where the exponent $\alpha_h = 5$ is a fitting parameter.

As already mentioned, the deformation capacity of corroded reinforcement bars is dramatically affected by corrosion. However, when the concept of engineering strain according to Equation (1) is used, the value of the ultimate strain (strain at the maximum force) of a corroded rebar has also been reported to depend strongly on the gauge length and the position of the extensometer (bridging or excluding the pit).[35] As a result, the ultimate strain measured across the corrosion pit and outside the pit region display clearly distinct relations with the corrosion level. This is evident in Figure 3c, where ε_u^{50} and $\varepsilon_u^{25\_out}$ are the ultimate strains measured with a 50 mm extensometer across the pit and with a 25 mm extensometer outside the pit, respectively. Note that for an extensometer placed outside the pit, the gauge length has no significant effect on the measured strain as long as it is greater than the rib spacing.[35]

While the strain across the pit decreases smoothly with increasing corrosion levels, a critical corrosion level exists beyond which the ultimate strain outside the pit exhibits a sudden drop. This can be explained by the fact that when the cross-section in the pit is reduced to a certain point, the maximum force reached in the pit is lower than the force required to reach yielding in the originally uncorroded cross-section. Based on that and as previously reported by Chen et al.,[35] the critical corrosion level, μ_{crit}, can be defined as:

$$\mu_{crit} = 1 - \frac{f_{y,0}}{f_{u,0}} \tag{6}$$

where $f_{y,0}$ and $f_{u,0}$ are the yield and ultimate strengths, respectively, of the uncorroded rebar. The empirical relations of ε_u^{50} and $\varepsilon_u^{25\_out}$ are[35]:

$$\varepsilon_u^{50}(\mu) = \varepsilon_{u_0}^{50} e^{-4.27\mu} \tag{7}$$

$$\varepsilon_u^{25out}(\mu) = \begin{cases} \varepsilon_{u_0}^{50} e^{-9.46\mu} & \mu < \mu_{crit} \\ \varepsilon_{u_0}^{50}(0.0262)(1-\mu) & \mu \geq \mu_{crit} \end{cases} \tag{8}$$

where $\varepsilon_{u_0}^{50} = 0.129$ is the ultimate strain of an uncorroded bar measured with a 50 mm gauge length extensometer. Note that $\varepsilon_{u_0}^{50}$ is also used in Equation (8) since this value of the ultimate strain outside of the pit region is in principle independent of the gauge length for an uncorroded rebar.

The last studied parameter of the mechanical behavior of corroded rebars was the strain at rupture, ε_r, which defines the end of the softening branch. As observed in Figure 2a, the variation of the strain at rupture followed a similar trend as the ultimate strain. Therefore, in

Figure 3d the ratio between these was investigated, where a moderate increase can be observed for increasing corrosion levels. Thus, the following expression is used to describe the variation of the strain at rupture with the corrosion level:

$$\varepsilon_{\mathrm{r}}(\mu) = \left[7.84\mu^2 + 1.6\right]\varepsilon_{\mathrm{u}}(\mu) \tag{9}$$

It is worth noting that the experimental results presented in Figure 2a and the expressions derived thereof are based on tests performed on bars with a single bar diameter. It is here assumed that the mentioned expressions can be extrapolated to other diameters, which needs to be experimentally validated.

2.2 | Mechanical model for steel bars with localized corrosion

Based on the expressions found in the previous section given by Equation (6)–(9), the following stress–strain constitutive law for steel reinforcement bars with localized corrosion is suggested:

$$\sigma(\varepsilon,\mu) = \begin{cases} \varepsilon_{\mathrm{s}} E_{\mathrm{s}} & \varepsilon_{\mathrm{s}} \leq \varepsilon_{y,0} \\ f_{y,0} & \varepsilon_{y,0} < \varepsilon_{\mathrm{s}} < \varepsilon_{\mathrm{sh}}(\mu) \\ f_{\mathrm{u},0} - \left(f_{\mathrm{u},0} - f_{y,0}\right)\left(\dfrac{\varepsilon_{\mathrm{u}}(\mu) - \varepsilon_{\mathrm{s}}}{\varepsilon_{\mathrm{u}}(\mu) - \varepsilon_{\mathrm{sh}}(\mu)}\right)^P & \varepsilon_{\mathrm{sh}}(\mu) \leq \varepsilon_{\mathrm{s}} \leq \varepsilon_{\mathrm{u}}(\mu) \\ f_{\mathrm{u},0} - \left(f_{\mathrm{u},0} - f_{\mathrm{r},0}\right)\left(\dfrac{\varepsilon_{\mathrm{s}} - \varepsilon_{\mathrm{u}}(\mu)}{\varepsilon_{\mathrm{r}}(\mu) - \varepsilon_{\mathrm{u}}(\mu)}\right)^3 & \varepsilon_{\mathrm{s}} > \varepsilon_{\mathrm{u}}(\mu) \end{cases} \tag{10}$$

where $E_{\mathrm{s}} = 200$ GPa is the steel Young's modulus which is assumed to remain constant based on the force–strain results shown in Figure 2a, $\varepsilon_{y,0} = f_{y,0}/E_{\mathrm{s}}$ is the yield strain of the uncorroded bar and P is the strain-hardening power, as defined by Equation (11)[41]:

$$P = E_{\mathrm{sh}_0}\frac{\varepsilon_{u_0} - \varepsilon_{\mathrm{sh}_0}}{f_{u_0} - f_{y_0}} \tag{11}$$

where E_{sh_0} is the tangent slope at the onset of strain-hardening, $\varepsilon_{\mathrm{sh}_0}$, also referred to as strain-hardening modulus. Based on the experimental results, the strain-hardening modulus can be estimated to vary between $0.013E_0$ and $0.014E_0$, which gives a value of P of approximately 2.5. The last expression in Equation (10) is suggested in this work to describe the postpeak branch of steel rebars in an analogous way as for the strain-hardening branch, where the exponent has been fitted to the experimental data.

Moreover, even though defining the exact moment when corroded bars yielded became difficult with increasing corrosion, the strain where a clear loss of linearity occurred was generally close to the yield strain of the uncorroded rebar. Therefore, the yield strength was used instead of the proof strength for the sake of simplicity, which was assumed constant and equal to the yield strength of the uncorroded rebar. This simplification is expected to introduce only a small error around the yield point.

In Figure 4, the proposed mechanical model is compared against the experimental results of bars with different levels of corrosion, which illustrate how the model can capture the progressive degradation of the stress–strain relationship for increasing corrosion levels. Moreover, it is worth mentioning that the proposed constitutive law given by Equation (10) could be easily implemented to describe the stress–strain relationship of corroded reinforcement in FE analyses where reinforcement is modeled as 1D elements.

3 | MODELING THE FLEXURAL BEHAVIOR OF CORRODED HYBRID-RC BEAMS

The model proposed in this work to evaluate the force–deflection response of a hybrid-RC beam (or slab's strip) with localized corrosion involves three main steps:

a. the discretization of the beam into a series of segments, each representing a nonlinear hinge.
b. the determination of the sectional behavior (moment–curvature) of each hinge.
c. the stepwise calculation of the force–deflection diagram.

Moreover, the proposed model also involves a number of assumptions. First, the pits are assumed to coincide with the position of transverse cracks, which has been shown to be a reasonable assumption before longitudinal cracking occurs.[18] As such, the model is mainly meant for the analysis of elements with dominant localized corrosion where corrosion-induced longitudinal cracking has not yet occurred. This is in line with the assumption that the length of existing pits is less than 50 mm, as corrosion distributed over longer regions increases the risk of longitudinal cracking. Similarly, the bond strength of the rebar-concrete interface is assumed to remain largely unaffected by pitting so that anchorage failure is prevented. In the following, a detailed description of the different steps involved in the modeling procedure is given.
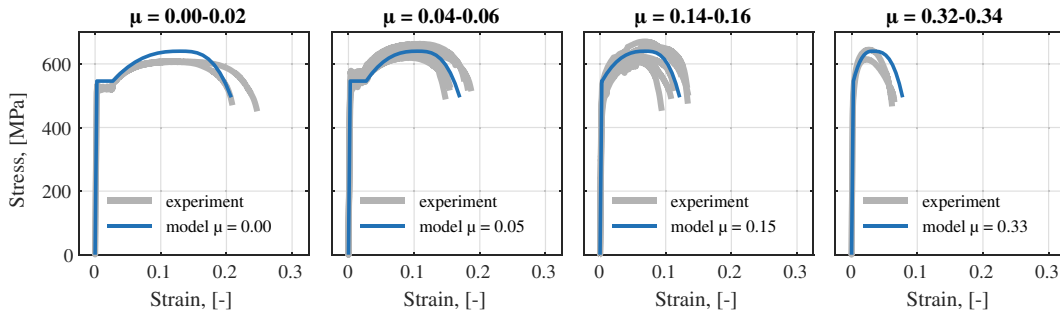
FIGURE 4 Comparison of the modeled stress–strain relationship for reinforcement bars with different local corrosion levels and experimental results from Chen et al.[35]
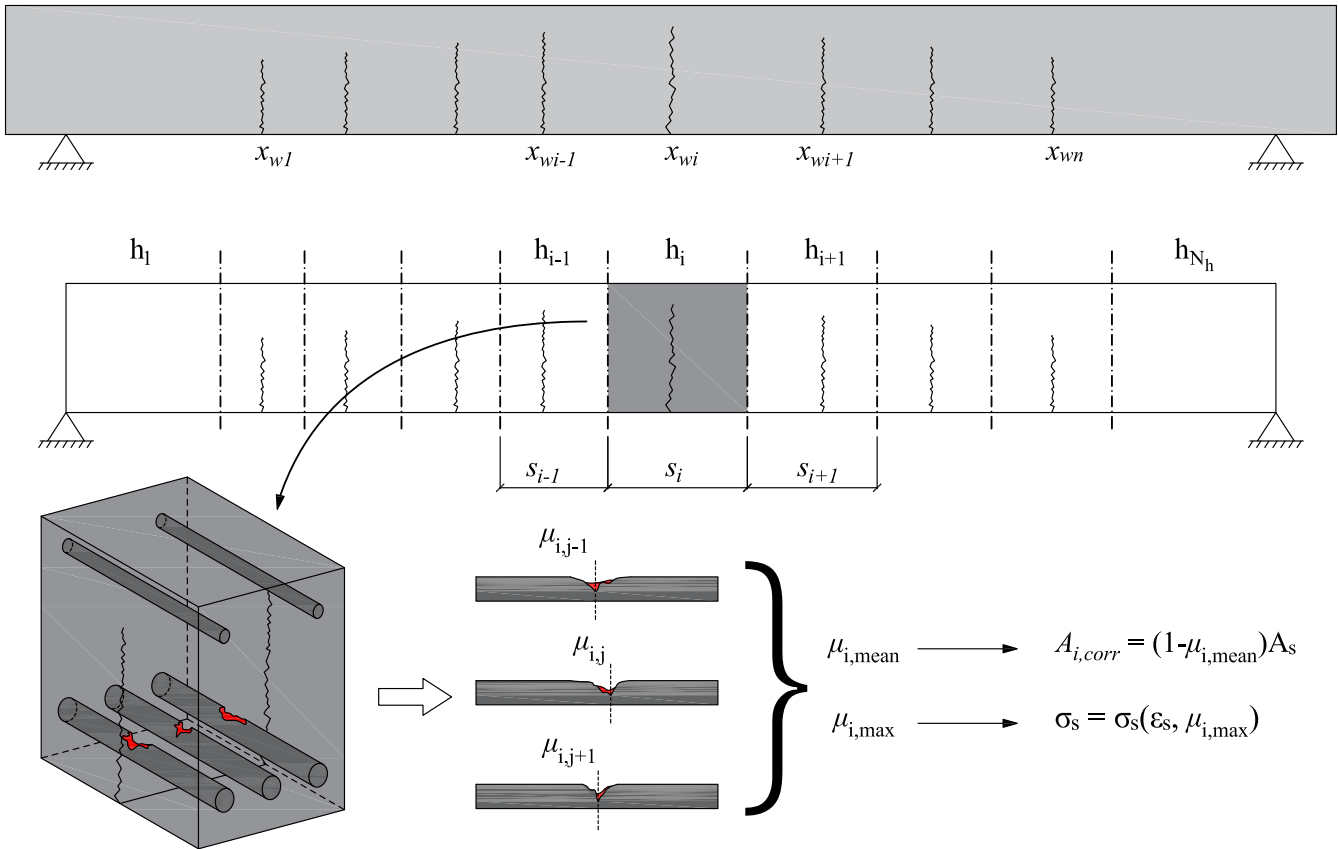
FIGURE 5 Discretization of a beam segment based on the position of existing cracks and determination of the average and maximum corrosion level in a hinge.

3.1 | Beam discretization and determination of corrosion input parameters

In the present study, a hinge is defined at the position of each of the major preexisting cracks in the beam. The boundaries of the hinge are then determined as the midpoint between the crack contained in the hinge and the two adjacent cracks. For the first and last crack, a symmetric hinge boundary is created based on the next and previous crack, respectively. Moreover, two additional

hinges are created at the ends of the beam, limited by the position of the supports. Figure 5 illustrates how a beam with a given crack distribution is discretized into N_h hinges.

Because the model presented in this study is meant for the assessment of corroded structures, the existing crack pattern is assumed available. Nevertheless, in the absence of the crack pattern, the model can be used assuming an average crack spacing calculated according to current design codes.[42] It should be noted that since the crack spacing may not be constant, this method

generally results in hinges of different length with a non-symmetric distribution.

By modeling the beam as a series of hinge elements, it is convenient to consider the local variation of stiffness along the beam due to localized pitting corrosion. To that end, every hinge can be described by its own moment–curvature relationship which depends on the corrosion level at the hinge. The cross-section of a beam is, however, always reinforced with several rebar where each rebar may be potentially affected to a very different extent by corrosion. For that reason, the model input regarding the corrosion level of each hinge needs to be determined. Corrosion affects both the load capacity and the deformation capacity of the hinge, but these two mechanisms are driven by different corrosion parameters. On the one hand, when the deformation capacity of the hinge is limited by the rupture of the reinforcement, the governing parameter is the maximum corrosion level of the most corroded rebar, as the failure of any of the bars can be also considered the failure of the hinge. On the other hand, the load capacity of the hinge is governed by the sum of the individual contributions of each rebar. Therefore, the following two corrosion parameters are defined:

$$\mu_{i,\max} = \max\left\{\mu_{i,j}\right\} \text{ for } j = 1, \ldots, n_{\text{bars}} \tag{12}$$

$$\mu_{i,\text{mean}} = \frac{1}{n_{\text{bars}}}\sum_{j=1}^{n_{\text{bars}}} \mu_{i,j} \tag{13}$$

where $\mu_{i,j}$ is the maximum corrosion level in the pit of the jth bar in the ith hinge, n_{bars} is the number of tensile reinforcement bars in the hinge, $\mu_{i,\max}$ is the maximum corrosion level at the ith hinge to be used in Equations (3)–(5) and Equations (7)–(10) and $\mu_{i,\text{mean}}$ is the average corrosion level of the bars at the ith hinge. It should be noted that the model requires knowledge about the maximum corrosion level at the pits of each hinge, which should be estimated based on best current existing practices. Alternatively, in the absence of detailed information, various corrosion scenarios may be investigated to evaluate the impact of localized corrosion on the global behavior of hybrid-RC beams.

3.1.1 | Cross-sectional analysis: Nonlinear hinge model for hybrid-RC

In the present work, a simplified model for sectional analysis based on the nonlinear hinge model as described by Löfgren[43] following the recommendations of RILEM TC 162-TDF[44] is adopted. In order to determine the distribution of stresses and strains in the cross-section, the following assumptions regarding the kinematics of the hinge are introduced:

a. The average strain in the reinforcement is related to the average elongation of the hinge at the level of the reinforcement.
b. Tension stiffening and the variation of stresses within the hinge element are not considered.
c. The crack surfaces remain plane and the crack opening angle, θ^*, equates the overall angular deformation of the nonlinear hinge.

The principle of the analysis for a structural element subjected to a combination of bending moment and axial force and the resulting distribution of strain and stress along the height of the hinge are shown in Figure 6.

The mean curvature of the hinge, χ_m, is given by:

$$\chi_m = \frac{\theta}{s} \tag{14}$$

where θ is the angular deformation, that is, the rotation of the hinge, which is assumed equal to the angular deformation of the crack, θ^*, and s is the length of the nonlinear hinge.

Based on the kinematic assumption, the average strain distribution is linear across the section height. Thus, at any horizontal layer of the hinge, the average longitudinal strain is expressed as:

$$\varepsilon(y) = \chi_m \cdot (y - y_0) \tag{15}$$

where y is the vertical coordinate measured from the top of the cross-section and y_0 is the depth of the neutral axis. The average strain at the bottom and top reinforcement can then be calculated as:

$$\varepsilon_s = \chi_m \cdot (d_s - y_0) \tag{16}$$

$$\varepsilon'_s = \chi_m \cdot (d'_s - y_0) \tag{17}$$

where d_s and d'_s denote the distance of the center of the bottom and top rebar, respectively, to the top surface of the beam, as depicted in Figure 6. The stress in the steel reinforcement can be calculated according to Equation (10), where the stress in tensile reinforcement $\sigma_s(\varepsilon_s, \mu_{\max})$ is a function of the maximum corrosion level in the hinge whereas the stress of the reinforcement in compression $\sigma'_s(\varepsilon'_s, 0)$ is based on the mechanical
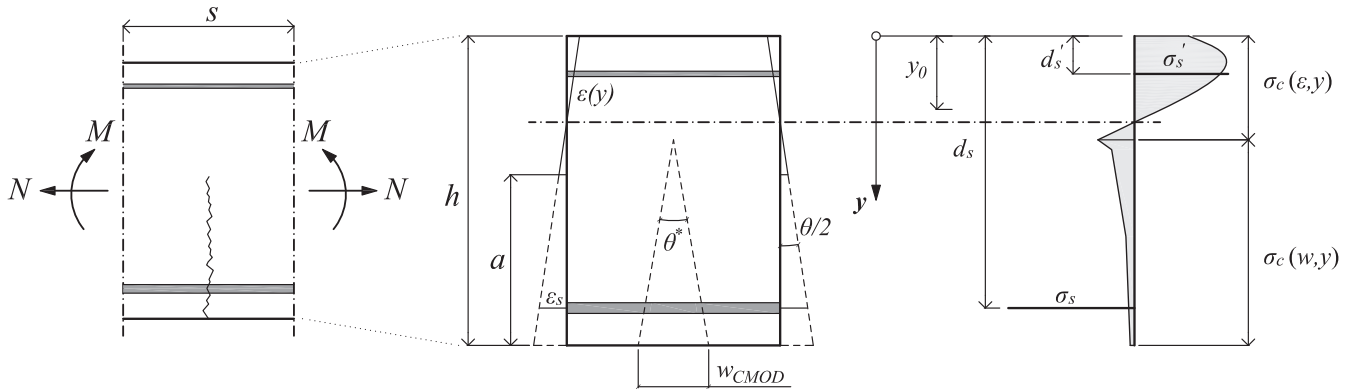
FIGURE 6 Principle of analysis for a structural element subjected to bending moment and axial force: kinematic relationships and stress and strain distribution in a cracked section.

behavior of an uncorroded rebar (i.e., the compressive reinforcement is assumed to be uncorroded).

It is important to recall that the stress–strain constitutive law defined by Equation (10) is based on the relations investigated using strain measurements with a 50 mm extensometer. However, as previously mentioned, the value of the ultimate strain is very sensitive to the gauge length used to measure it. To address this issue, a semi-analytical model proposed by Chen et al.[35] is used to calculate the ultimate strain over any gauge length l_g greater than 50 mm, where the pit length is assumed smaller than 50 mm:

$$\varepsilon_u^{l_g}(\mu_{max}) = \frac{50\varepsilon_u^{50}(\mu_{max}) + (l_g - 50)\varepsilon_u^{25_{out}}(\mu_{max})}{l_g} \quad (18)$$

where ε_u^{50} and $\varepsilon_u^{25\_out}$ are the values defined by Equations (7) and (8), respectively, and the gauge length $l_g = s$ is given in mm. The adjusted ultimate strain, $\varepsilon_u^{l_g}$, is then used in Equation (10) to account for the influence of the hinge length on the ultimate strain of the corroded rebar segment.

In the compressive zone of the hinge, where $y \leq y_0$, the stresses in the concrete are related to the strain through the constitutive law of concrete under compression, $\sigma_c(\varepsilon)$. In this study, the model proposed by Thorenfeldt et al.[45] was chosen to describe the complete stress–strain relationship of plain concrete under compression. For FRC in compression, however, it has been experimentally observed that the fibers provide a slower postpeak degradation. Consequently, the constitutive law proposed by Ruiz et al.[46] was used. Both models are illustrated in Figure 7a. It should be noted that the postpeak branch of both models is modified as shown in Figure 7b to account for the size effect of the hinge length compared to reference fracture zone in a 300 mm cylinder.[47]

In the tensile zone of the hinge, $y \geq y_0$, the concrete is assumed to remain linear until the tensile strength of the concrete, f_{ct}, is reached. Thereafter, a cohesive law or stress-crack opening relationship is used to describe the postcracking stress:

$$\sigma_c = \begin{cases} \varepsilon(y) \cdot E_c, & \varepsilon(y) \leq f_{ct}/E_c \\ \sigma_{ct}(w(y)), & \varepsilon(y) > f_{ct}/E_c \end{cases} \quad (19)$$

where E_c is the modulus of elasticity of the concrete and $w(y)$ is the crack width along the height of the crack, which can be approximated by Equation (20):

$$w(y) = \left[\chi_m(y - y_0) - \frac{f_{ct}}{E_c}\right] \cdot s \quad (20)$$

The contribution of the process zone in plain concrete is considered negligible and, consequently, cracks are considered stress-free after the concrete reaches its tensile strength, that is, $\sigma_{ct}(w) = 0$. Conversely, the postpeak behavior of FRC in tension is described by a stress-crack opening relationship in the form of a multilinear curve according to Equation (21):

$$\sigma_{ct}(w) = \left[\alpha_i + (\alpha_{i+1} - \alpha_i)\frac{w - w_i}{w_{i+1} - w_i}\right]f_{ct} \quad \text{for } w_i < w \leq w_{i+1} \quad (21)$$

where $\alpha_i = \sigma_i/f_{ct}$ is the stress corresponding to the crack width w_i normalized with respect to the tensile strength of the concrete and w_u is the ultimate crack width beyond which the crack becomes stress-free. The constitutive relationship of concrete in tension for plain concrete and FRC are illustrated in Figure 8. It is worth mentioning that in the past, either drop-constant or bilinear-
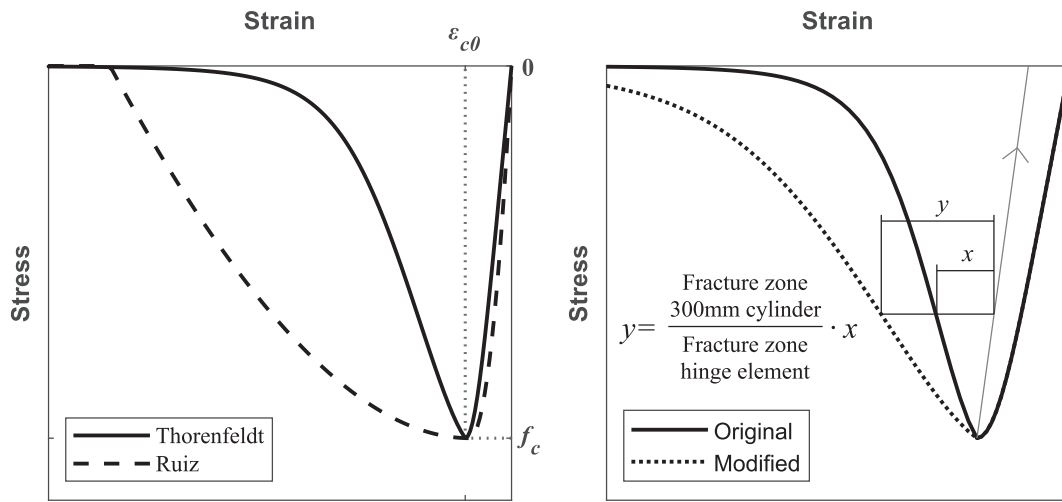
FIGURE 7 (a) Thorenfeldt et al.[45] and Ruiz et al.[46] models for the constitutive law of concrete and FRC, respectively, in compression. (b) Example of modified Thorenfeldt constitutive law accounting for the size effect of the hinge length, after Hanjari et al.[47]
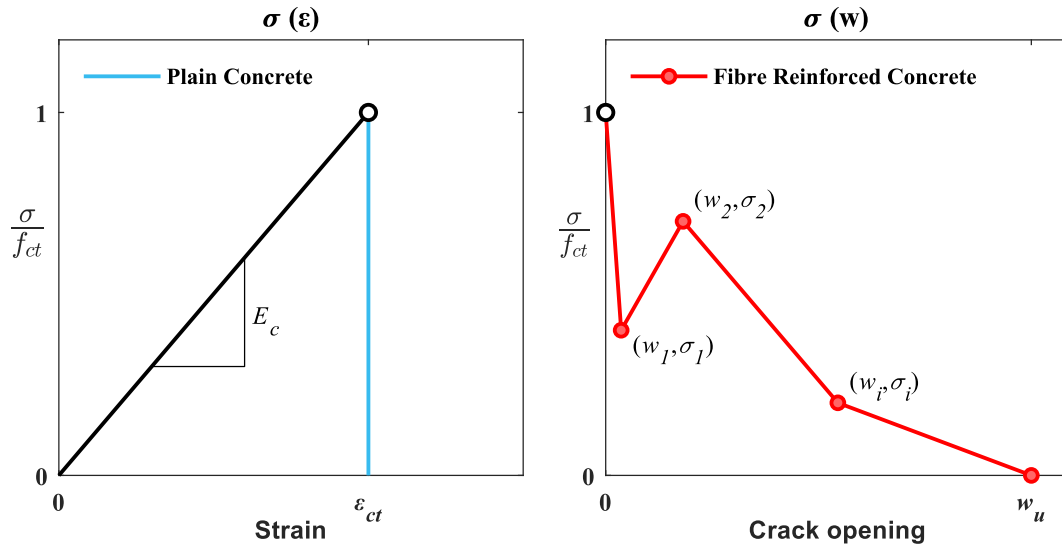

FIGURE 8 Tensile behavior of concrete in tension: (a) linear stress–strain relationship in tension before cracking and perfectly brittle behavior assumed for plain concrete after cracking; (b) example of a possible FRC postcracking stress-crack width relationship described by a multilinear curve with four branches.

relationships have been adopted to describe the post-cracking response of FRC, which enabled obtaining closed-form solutions for the curvature-moment relationship of the section. However, according to Barros et al.,[48] four branches of a multilinear stress-crack opening relationship are needed to describe with sufficient accuracy the postcracking behavior of most FRC mixes used in practice. Therefore, in this work, the number of branches of the multilinear stress-crack opening relationship can be selected as an input parameter. It is worth mentioning that the mechanical degradation of FRC due to corrosion, which has been experimentally observed and discussed by several, see for example,[49–51] was not considered in

the model due to the current lack of comprehensive understanding and experience. However, including this phenomenon in the model is straightforward provided the constitutive law of the FRC with fiber corrosion is available in the future.

Once the stress over the height of the hinge section is determined, the internal axial force and bending moment can be calculated according to Equations (22) and (23):

$$N_{\text{int}} = \int_0^{h-a} \sigma_{\text{c}}(y) \cdot b(y) \cdot dy + \int_{h-a}^{h} \sigma_{\text{ct}}(w(y)) \cdot b(y) \cdot dy + \sigma_{\text{s}}(1 - \mu_{\text{mean}})A_{\text{s}} + \sigma'_{\text{s}}A'_{\text{s}} \tag{22}$$
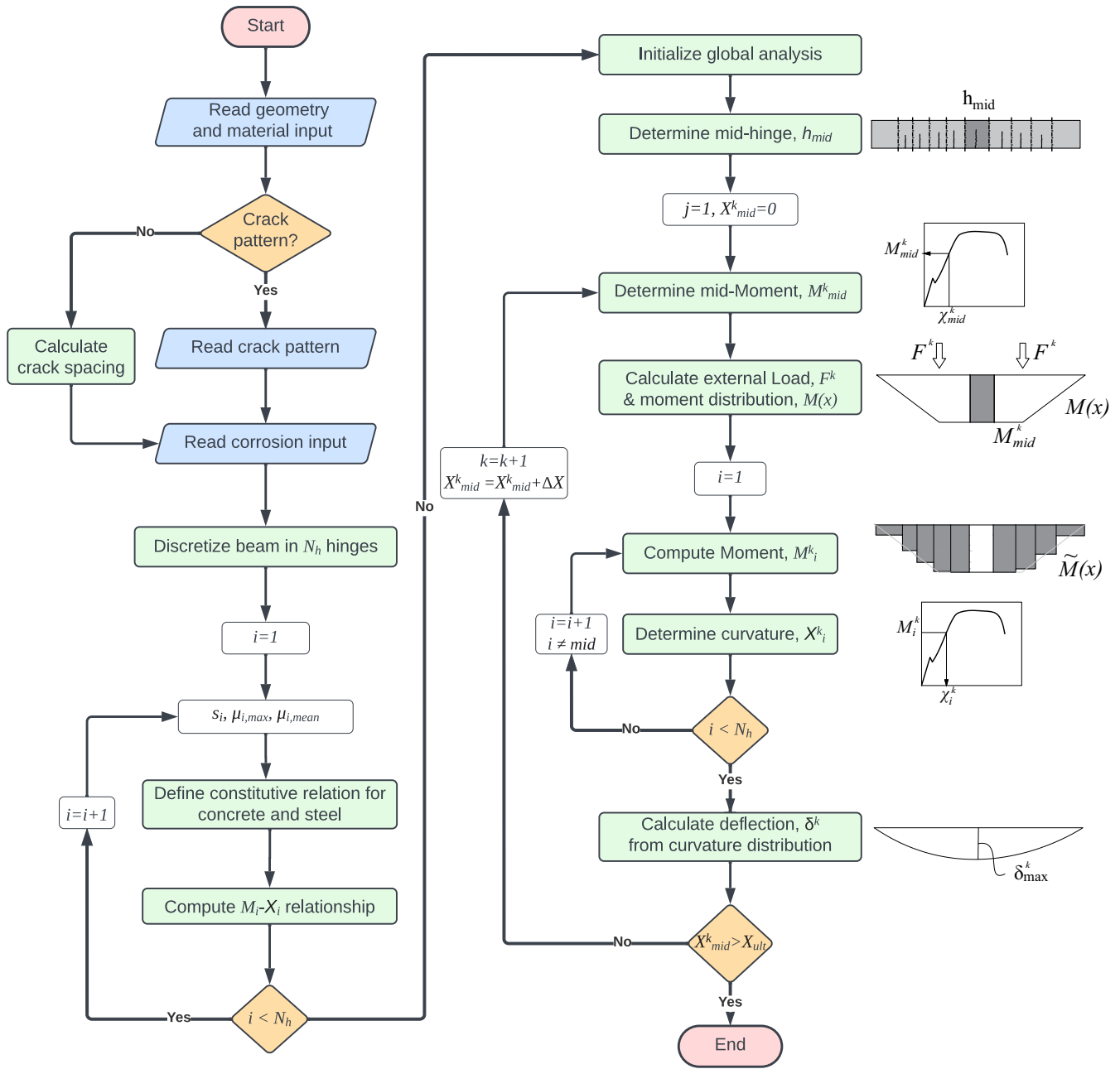
FIGURE 9 Analysis procedure of the proposed model for the calculation of the force–deflection diagram of statically determined beams with localized reinforcement corrosion.

$$M_{int} = \int_0^{h-a} \sigma_c(y) \cdot y \cdot b(y) \cdot dy + \int_{h-a}^{h} \sigma_{ct}(w(y)) \cdot y \cdot b(y) \cdot dy + \sigma_s(1 - \mu_{mean})A_s d_s + \sigma'_s A'_s d'_s$$

(23)

where A_s and A'_s are the cross-sectional areas of the tension and compression reinforcement, respectively and a is the crack height, as illustrated in Figure 6.

The procedure used to obtain the cross-sectional response of the hinge element and the moment–curvature diagram follows an iterative approach. For a given curvature, or rotation, of the hinge, the position of the neutral axis y_0 is found from Equation (22) by imposing the force equilibrium condition $N_{int} - N_{ext} = 0$. Once the position of the neutral axis is known, Equation (23) gives the corresponding bending moment. By progressively increasing the value of the curvature, the entire moment–curvature diagram of the hinge can be obtained. In this model, the sectional analysis of a hinge is interrupted when the strain in the reinforcement exceeds the ultimate strain of the steel (steel rupture) or when

equilibrium can no longer be reached due to insufficient capacity in the concrete (concrete crushing).

3.2 | Global analysis: Procedure for the evaluation of the force–deflection relationship

The analysis procedure presented in this section and illustrated in Figure 9 is valid for statically determinate beams simply supported on both ends and failing in bending. However, the procedure may be adapted with minor modifications to other types of statically determinate beams, for example, cantilever beams. Once the crack pattern is determined and the beam is discretized into N_h hinges, the moment–curvature $M_i(\chi_i)$ relationship of each hinge is first calculated based on the geometry, material and corrosion input parameters $\left(\mu_{i,j}\right)$ of the hinge. Next, the global analysis is initialized by incrementally varying the curvature of one of the hinges. In this study, the hinge chosen to steer the analysis is the one where the largest bending moment is expected to occur. Since the midspan of a simply supported beam is the most loaded section for symmetrical load distributions, the analysis is steered using the mid-hinge, denoted as h_{mid}, which is defined as the hinge closest to the mid-span coordinate. At the kth loading step, the sectional moment at the mid-hinge M_{mid}^k is obtained from the moment–curvature relationship of the mid-hinge, $M_{mid}(\chi_{mid})$.

For statically determined beams, the shape of the moment distribution is only a function of the number of external loads and their position while the magnitude of the moment distribution is proportional to the magnitude of those loads. Assuming that the ratio between the magnitude of the loads is kept constant when more than one point load acts on the beam, the entire moment distribution can be obtained if the moment at one single point of the distribution is known. Therefore, M_{mid}^k is used to find the theoretical moment distribution at the kth loading step, $M(x)$, which in turn can be used to determine the sectional moment at each of the remaining hinges, where M_i^k ($i=1,...,N_h; i\neq mid$) is the moment of the ith hinge at the kth loading step.

Subsequently, the corresponding curvature of every hinge, χ_i^k, can be obtained from the corresponding moment–curvature relationship, $M_i(\chi_i)$, of each hinge. It should be noted that the curvature may not be unequivocally determined from the bending moment due to the existence of one or more descending branches in the moment–curvature diagram. In that case, the curvature is determined as the smallest of all curvatures with the target moment, provided the moment of the hinge in the

kth step is greater than the moment in any previous step, $M_i^k > M_i^{1:k-1}$. If the previous condition is not fulfilled, it means that the steering hinge is advancing through a descending branch of the moment–curvature diagram which entails that rotation localizes in the mid-hinge and the remaining hinges undergo unloading. However, to avoid returning elastically by the original loading path, an unloading path must be defined. Since unloading/reloading was not defined at the material level in this work, a simplified approach is adopted to account for the unloading and reloading of the hinges according to Equation (24):

$$\chi_i^k = \chi_i^{k-1} + \left(M_i^k - M_i^{k-1}\right)/K_{unload} \qquad (24)$$

where K_{unload} is the bending stiffness of the hinge upon unloading/reloading, which can be chosen to describe the intended behavior of the hinge from full elastic recovery $\left(K_{unload} = M_i^{k-1}/\chi_i^{k-1}\right)$ to fully inelastic $\left(\chi_i^k = \chi_i^{k-1} \text{ when } K_{unload} \to \infty\right)$. In this study, K_{unload} was given an intermediate value of $10 \cdot K_{II}$, where K_{II} is the average bending stiffness of the hinge in state II, that is, after cracking and before yielding of the reinforcement.

To calculate the rotation and deflection distribution, an auxiliary mesh of element size Δx is generated along the beam. This step is implemented to obtain the rotation and deflection at specific locations, for example, at midspan and avoid having to interpolate the results later. Each element is assigned the curvature of the hinge in which the element is positioned. Subsequently, the curvature of the auxiliary mesh, $\chi'(x)$, is integrated, in its discrete form, once to obtain the rotations and once more to obtain the deflections according to:

$$\theta(x) = \sum_{i=1}^{x/\Delta x} \left(\chi'(x_i) \cdot \Delta x\right) + C_1 \qquad (25)$$

$$\delta(x) = \sum_{i=1}^{x/\Delta x} \left(\theta(x_i) \cdot \Delta x\right) + C_1 \cdot x_i + C_2 \qquad (26)$$

where $\theta(x)$ and $\delta(x)$ are the rotation and deflection distributions, respectively, and C_1 and C_2 are integration constants determined by the boundary conditions.

4 | MODEL EVALUATION

In this section, the performance of the proposed model is evaluated in terms of its ability to predict the global load-deflection behavior of four beams tested experimentally by the authors in previous studies.[18,52]
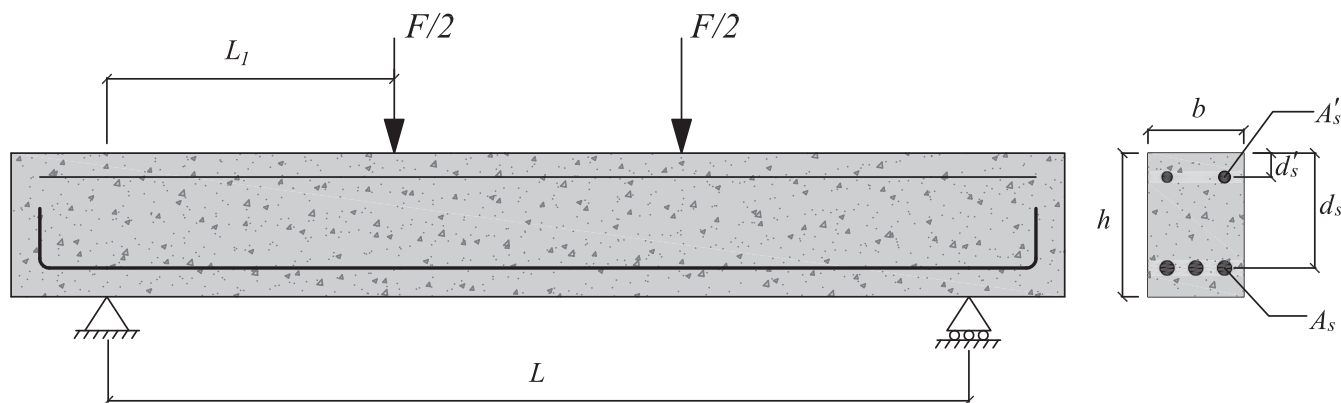
FIGURE 10 Definition of parameters describing the geometry and reinforcement of a reinforced concrete beam. Data for the different beams is included in Table 1.

Two RC and two hybrid-RC beams were investigated, where one of the beams in each group was uncorroded and the other presented pitting corrosion. The hybrid-RC beams, that is, Beam2 and Beam4, included a fiber dosage of 0.25% vol. (20 kg/m^3) and 0.5% vol. (40 kg/m^3) of steel fibers, respectively. The fiber type used in both cases was a hooked-end steel fiber Dramix 3D from Bekaert with a length of 35 mm a diameter of 0.55 mm. The stress-crack width opening relation of the fiber reinforced concrete matrix was obtained through an inverse analysis of wedge-splitting tests and three point bending beam tests for Beam2 and Beam4, respectively, as described.[53,54] The beams with localized pitting corrosion, namely Beam3 and Beam4, were corroded through cyclic exposure to a chloride solution with a 16.5% NaCl concentration for 3 years while loaded under three-point bending to achieve a maximum crack width opening of 0.2 mm at the surface. After loading the beams to failure, the rebars were extracted and the maximum local corrosion level in the pits was determined by 3D-scanning, obtaining a detailed description of the residual cross-sectional area which was then corrected to account for the area reduction due to necking as described.[18]

Since the beams were tested in different experimental programs, the geometry and material properties of the concrete and the reinforcement as well as the load configuration varied among the beams. Moreover, the actual crack pattern, which was carefully documented for the corroded beams is used as input for Beam3 and Beam4 whereas an average crack spacing is used as input for Beam1 and Beam2. Figure 10 illustrates the parameterized geometry and reinforcement layout of a typical reinforced concrete beam loaded in four point bending configuration while the input values for each parameter is given in Table 1 for the different beams investigated.

In Figure 11, a comparison is presented between the experimentally determined force–deflection response (black lines) and the response predicted by the proposed model according to the data presented in Table 1 (blue markers) for the four investigated beams. Note that for Beam1, results from five identical specimens were available, which have been included to illustrate the dispersion in the tests.

As observed, the model was able to reproduce the global response of the uncorroded beams, Beam1 and Beam2, with very good agreement. Particularly, the model was able to capture both the failure mode (concrete crushing) as well as the ultimate deflection of Beam1 with great accuracy. Similarly, the model was also able to reproduce the behavior of Beam2, although in this test the beam was unloaded before failure even though the analysis shows that a larger deflection could have been reached.
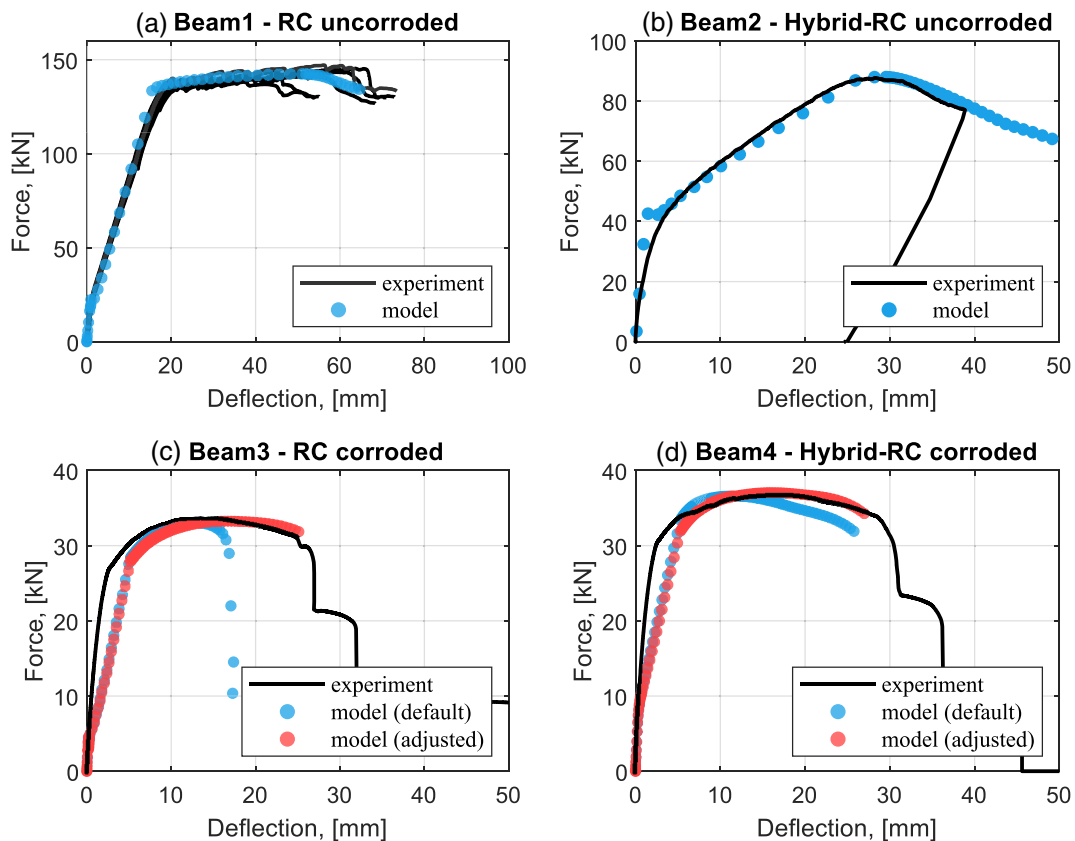
On the other hand, the model did not show the same level of agreement between the predicted and experimentally determined response for the corroded beams when using the input values given in Table 1. It is worth mentioning that the differences observed on the initial ascending branch can be attributed to the fact that the tested beams were preloaded to induce cracking before and during exposure to wetting and drying cycles in chloride solution. On the other hand, the main source of disagreement in the postpeak behavior was not corrosion itself, but rather the particular geometry of the shallow beams.

Looking at Beam3 in Figure 11c, it can be observed that the model captured well the maximum load capacity, although the predicted failure mode was concrete crushing failure instead of the actual steel rupture and the maximum deflection was significantly underestimated by the model. After investigating the possible causes for the disagreement, it was determined that the most likely explanation was the localization of concrete crushing into

TABLE 1 Summary of input data for the model.

|		Beam1	Beam2	Beam3	Beam4
General description					
Reference		n/a	Löfgren[52]	Berrocal et al.[18]	Berrocal et al.[18]
Reinforcement		Conventional	Hybrid	Conventional	Hybrid
Corrosion		No	No	Yes	Yes
Load setup		4-PBT	4-PBT	3-PBT	3-PBT
Geometry and reinforcement					
L	(mm)	2700	3750	1000	1000
L_1	(mm)	900	1250	500	500
h	(mm)	250	250	100	100
b	(mm)	200	750	180	180
d_s	(mm)	209	225	65	65
d'_s	(mm)	38	–	–	–
A_s	(mm²)	603	192	235	235
A'_s	(mm²)	157	–	–	–
Concrete input parameters					
f_{cc}	(MPa)	65.0	46.1	67.2	67.2
ε_{c0}	(−)	0.003	0.00275	0.0026	0.0026
f_{ct}	(MPa)	4.2	3.3	3.6	3.6
E_c	(GPa)	28.0	32.7	32.0	32.0
$\alpha f_{ct} - w$	(MPa, mm)	n/a	0.516f_{ct}, 0.02 0, 7.88	n/a	0.597f_{ct}, 0.043 0, 5.34
Steel input parameters					
ε_{sh_0}	(−)	0.027	0.027	0.027	0.027
ε_{u0}	(−)	0.129	0.07	0.129	0.129
f_{y0}	(MPa)	546	737	530	530
f_{u0}	(MPa)	626	835	640	640
f_{r0}	(MPa)	490	700	495	495
E_s	(GPa)	200	194	200	200
Crack pattern and corrosion input					
x_{cr} (μ_{mean}, μ_{max})	(mm) ([−], [−])	180 (0,0) ... s_r = 130 mm ... 2520 (0,0)	140 (0,0) ... s_r = 165 mm ... 3625 (0,0)	100 (0, 0) 200 (0, 0) 321 (0.03, 0.091) 406 (0.073, 0.139) 516 (0.124, 0.172) 626 (0, 0) 734 (0, 0) 806 (0, 0) 900 (0, 0)	100 (0, 0) 180 (0, 0) 241 (0, 0) 343 (0, 0) 395 (0, 0) 464 (0, 0) 535 (0.142, 0.174) 625 (0, 0) 711 (0, 0) 784 (0, 0) 820 (0, 0) 900 (0, 0)

FIGURE 11 Comparison of the force–deflection diagram between experimental results from bending tests and model prediction for: (a) Beam1—uncorroded RC beam; (b) Beam2—uncorroded hybrid-RC slab strip; (c) Beam3—corroded RC shallow beam; and (d) Beam4—corroded hybrid-RC shallow beam. Note that the scales are varying.

a zone that was shorter than the hinge length. As explained in Section 3.2, the postpeak behavior of concrete in compression is adjusted based on the hinge length to describe the deformation capacity of the concrete in compression. However, this corresponds to an assumption that the fracture region in the compression zone equals the entire hinge length. As shown in Figure 12, this assumption is applicable for Beam1, where the concrete crushing spreads beyond one single hinge. However, in Beam3 the fracture zone localized in a much narrower distance under the loading plate, which was approximately half the hinge length. By introducing an adjusted hinge length equal to $s^* = 0.5s$ in the calculation of the constitutive law of concrete in compression, the predicted response of the model (red markers in Figure 11c) achieved a much better agreement with the experimental results. It must be noted that even though crushing of concrete did occur in the experiments, it was not considered the failure mode of the beam because the deflection could still be increased without a significant loss of load capacity.

For Beam4, the force–deflection response initially predicted by the model also deviated slightly from the

experimental results. However, in this case, the main reason for the difference was attributed to the stress-crack opening relationship used to describe the post-cracking behavior of FRC. The stress-crack opening relationship was determined by inverse analysis from bending tests in beams with a 150 × 150 mm cross-section. However, Beam4 had a clear cover of only 30 mm which represented almost a third of the total height of the beam. It is possible that due to the well-known 'wall effect' through which fibers flowing in the concrete tend to orient themselves parallel to the walls of the form, the distribution and orientation of the fibers in the cover of Beam4 differed from the one in the material test beams. Alternatively, it may also be possible that a bilinear relationship was not sufficient to describe accurately the postcracking behavior of the mix used. To that end, the following new relationship with five branches was determined through inverse analysis using the proposed model which provided a better agreement, as shown by the red markers in Figure 11d: $(\alpha f_{ct}, w) = [(0.417 f_{ct}, 0.05 \text{ mm}), (0.417 f_{ct}, 2 \text{ mm}), (0.278 f_{ct}, 5 \text{ mm}), (0.139 f_{ct}, 10 \text{ mm}), (0, 12 \text{ mm})]$.

Beam1   Beam3
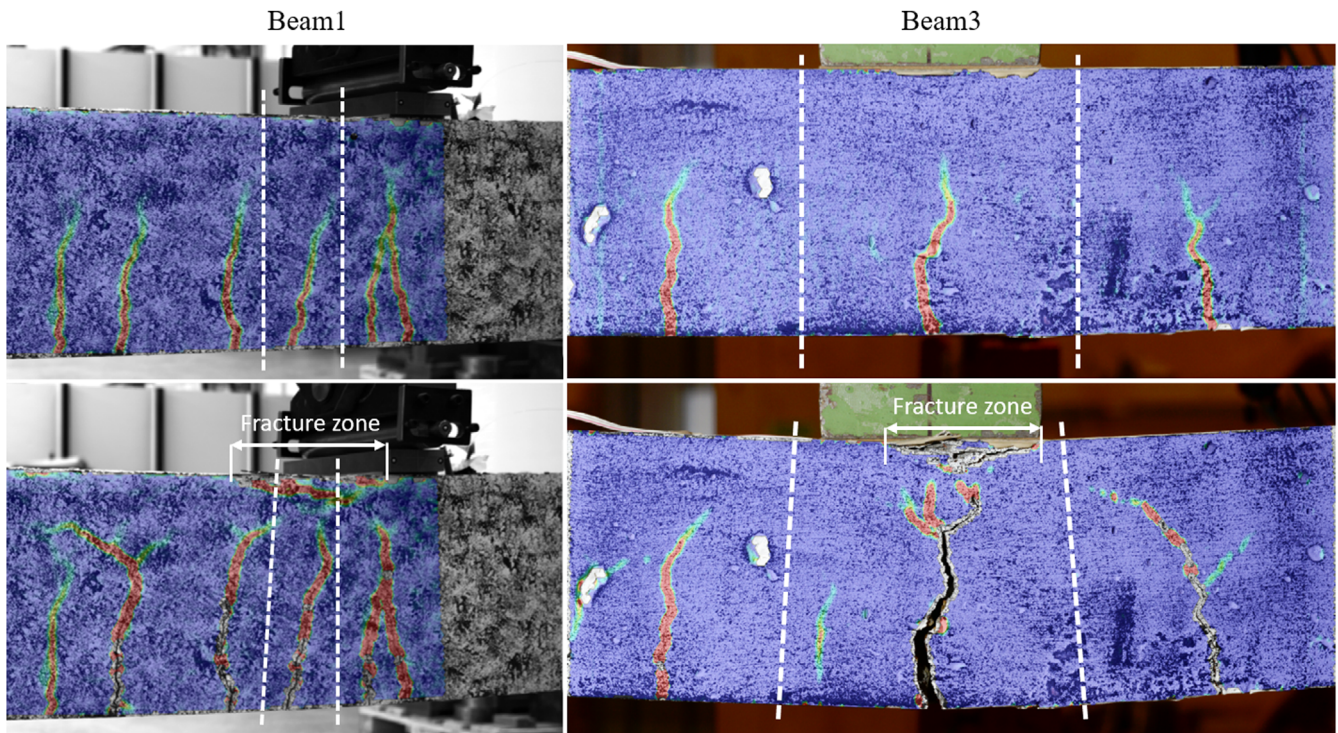
FIGURE 12 Horizontal strain field obtained by DIC from Beam1 and Beam3 during the loading test. The top images show the crack pattern at a load of 40 and 12 kN, respectively. The bottom images show the strain field after crushing of concrete in the compression zone has occurred. The fracture zone is indicated by a double-headed arrow whereas the dashed lines indicate the approximate position of the hinge boundaries.

5 | PARAMETRIC STUDY

The proposed model is used in this section to assess the influence of several parameters on the load-carrying and deformation capacity of hybrid-RC beams with localized corrosion. For that purpose, three main aspects are investigated:

i. The influence of a localized corrosion pit with increasing corrosion levels located at the most loaded section of a beam
ii. The role of the postcracking performance of FRC when fiber volume fractions are progressively increased
iii. The effect of corrosion distribution, going from one single pit to uniformly distributed corrosion, for increasing corrosion levels.

The parametric study is applied to simply supported beams with the reference geometry of Beam1 in Table 1. The material properties of the steel reinforcement and the concrete as well as the loading configuration were also adopted according to Beam1 in Table 1. However, since the load and deformation capacity of a beam are strongly influenced by the amount of tensile reinforcement, two different reinforcement layouts were used to include the effect of the reinforcement ratio, namely a low reinforcement ratio with 4Ø8 mm ($\rho_s \approx 0.48$) and a high reinforcement ratio with 4Ø16 mm ($\rho_s \approx 1.91$). Similarly, for each reinforcement ratio, two cases were investigated, a RC beam and a hybrid-RC beam, where the postcracking behavior of the FRC is described by the following relationship corresponding to a 0.5% vol. fiber dosage according to Jansson et al.[52]: (αf_{ct}, w) = [(0.35f_{ct}, 0.035 mm), (0.1f_{ct}, 3 mm), (0, 10 mm)].

5.1 | Effect of a localized corrosion pit with increasing corrosion level

To study the effect of a localized corrosion pit, the reference beam was divided into 21 hinges distributed symmetrically along the beam. In the mid-hinge, the corrosion level of the four tensile bars was varied between 0 and 0.5. The same corrosion level was set for all the bars; thus, the average and maximum corrosion levels were the same $\mu_{mid,mean} = \mu_{mid,max}$. The remaining hinges were assumed uncorroded.

In Figure 13, the relationship between the maximum corrosion level in the pit and the ultimate deflection and
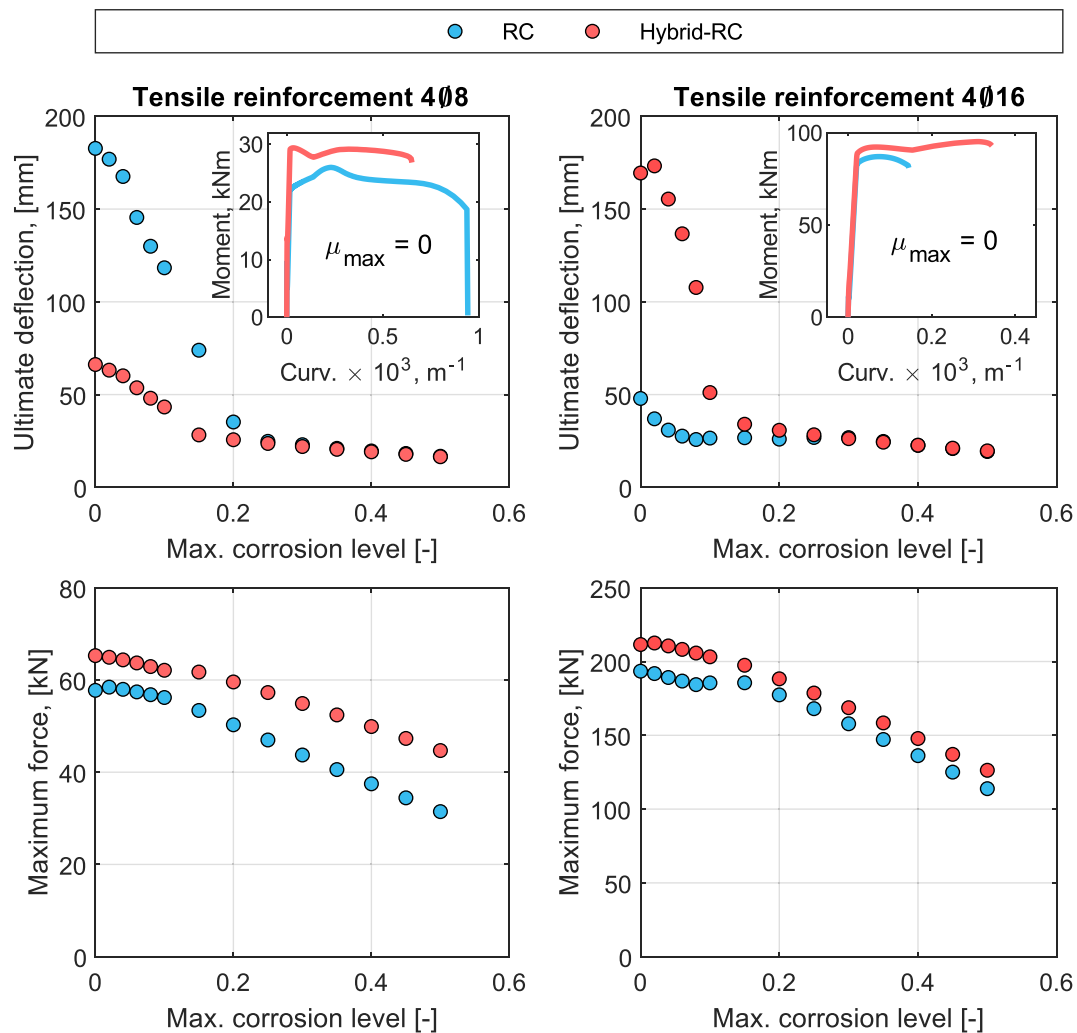
FIGURE 13 Numerical results of the ultimate deflection and maximum force as a function of the maximum corrosion level applied into a single corrosion pit in the center of the beam for RC and hybrid-RC beams with two different reinforcement ratios. The moment curvature for the uncorrected case is included for the four studied beams.

maximum load achieved is compared for the different beam configurations investigated. Regarding the load capacity, the results presented in Figure 13 agree with the expected response for which the load decreases proportionally to the corrosion level. The contribution of the fibers to the maximum load capacity is very limited for the beam with a high reinforcement ratio whereas a significantly higher load gain is observed for the beam with a low reinforcement ratio, particularly for higher corrosion levels.

The deformation capacity of the beams, on the other hand, displayed clearly different behaviors depending on the reinforcement ratio, the presence of fibers and the corrosion level. In the absence of corrosion, the RC beam with a lower reinforcement ratio exhibited a ductile behavior whereas the ultimate deflection of the hybrid-RC was significantly lower. Conversely, the hybrid-RC beam with a higher reinforcement ratio displayed a much

larger ultimate deflection than the RC counterpart in the uncorroded state.

The differences observed can be explained by looking at the corresponding moment–curvature diagrams, which are included in Figure 13 for the case where no corrosion is considered. The limited deformation capacity of the hybrid-RC beam with low reinforcement ratio can be attributed to the localization of rotation in one single hinge. This behavior is due to the relatively high contribution of the fibers to the load capacity of the beam, specially at smaller deflections, which causes that the maximum moment in the hinge occurs when the tensile reinforcement yields. After yielding, a further increase of curvature results in a decrease of moment due to the rapid loss of load contribution from the fibers, which causes the rest of hinges to unload.[55] Conversely, the maximum moment in the RC beam with low reinforcement ratio happens for a curvature well beyond the

yielding point, which enables all the hinges in the constant moment region to reach a larger rotation before unloading, thus contributing significantly to the ultimate deflection of the beam.

For the case with high reinforcement ratio, however, the RC beam exhibited a limited rotation capacity due to early concrete crushing. The addition of fibers granted the concrete an increased ductility in compression which allowed a certain amount of hardening of the tensile reinforcement to develop before concrete crushing occurred, thereby providing a significant additional rotation capacity and consequently a larger ultimate deflection.

Regarding the effect of corrosion, it is interesting to note how the ultimate deflection decreases rapidly in all cases until the maximum corrosion level reaches approximately between 0.15 and 0.2. For greater corrosion levels, the ultimate deflection keeps decreasing at a much lower rate but with virtually no difference between all the beams. This observation suggests that when the local corrosion exceeds 0.2, the ultimate deflection of the beam is mainly governed by the mechanical behavior of the corroded rebar, which is supported by the fact that the failure mode for all cases with a corrosion level equal or greater than 0.25 was steel rupture.

5.2 | The role of the postcracking behavior of FRC in hybrid-RC beams

The effect of varying the fiber dosage in hybrid-RC beams was investigated using the same beam geometry, material properties and loading configuration as in Section 5.1 but modifying the stress-crack width opening relationship of the FRC. In order to provide a realistic input for the model, the results from Jansson et al.[52] were used to fit three stress-crack width opening relationships for three different fiber dosages, namely 0.25%, 0.5%, and 1.0% vol. Thereafter, additional stress-crack width opening relationships were generated by interpolation of the fitted values at intermediate levels. In all cases, the stress-crack width relationships were defined with three linear branches. The experimental, fitted and interpolated stress-crack width opening relationships used for the parametric study are presented in Figure 14. A detail is included in Figure 14 to illustrate that using three branches for the entire postcracking behavior leads to an inaccurate description of the stress contribution of FRC at very small crack widths. Nevertheless, the proposed relationships were considered sufficient for a comparative study.

The exact values used to define the postcracking behavior of the different interpolated FRC were calculated as a function of the fiber volume fraction, ν_f, given in percentage, according to Equation (27):

$$
\begin{aligned}
\alpha_1(v) &= 0.267v_f^2 + 0.6v_f - 0.0167 \\
w_1(v) &= -0.013v_f^2 - 0.01v_f + 0.043 \\
\alpha_2(v) &= 0.4v_f^2 - 0.1v_f + 0.05 \\
w_2(v) &= 3\alpha_3(v) = 0w_3(v) = 10
\end{aligned}
\tag{27}
$$

It must be noted that even though increasing the fiber content in an hybrid-RC beam may result in the formation of more closely spaced cracks, this effect was not considered in the present study. However, to account for the stochastic nature of the crack formation process and its impact on the hinge length, each case was simulated 10 times with different crack patterns generated by selecting a random crack spacing between 100 and 160 mm. The maximum load and ultimate deflection of the beams with low and high reinforcement ratios are presented in Figure 15 together with the moment–curvature relationships for some of the fiber contents investigated.

For the beam with a low reinforcement ratio, there seems to be a certain fiber content threshold, around 0.4%–0.5% vol., above which a distinct change in global response can be observed. Indeed, for very small fiber contents, a positive effect can be seen on both the maximum force and ultimate deflection, very limited for the former and noticeably higher for the latter. This effect can be attributed to the ability of the fibers to prevent the quick degradation of the postpeak stress of the concrete in compression, which does not result in a significant increase of the maximum moment, but does increase the curvature at which it happens, thus enabling a larger rotation of the hinges in the constant moment region. Whereas a further increase of fiber content provides a certain increase of the load capacity, as previously discussed, the curvature associated to the maximum moment shifts toward the curvature at which reinforcement yielding happens, thus concentrating most of the rotation in a single hinge.

For the beam with a high reinforcement ratio, the results display a trend similar to the one observed for the low reinforcement ratio although with some differences. First, there is no fiber content above which the response of the beam changes significantly, although it might still occur at even higher fiber contents. Consequently, the effect of increasing the fiber content is less pronounced and more gradual for both the load and deformation capacity. A similar behavior is also observed between the low and high reinforcement ratio beams for the ultimate deflection when transitioning from RC to hybrid-RC. However, because the failure mode in the high reinforcement ratio beam is concrete crushing, the effect of adding a very small fiber dosage results in a large increase of deformation capacity. As previously explained, this

FIGURE 14 Experimental, fitted and interpolated stress-crack width opening relationships used in the parametric study.
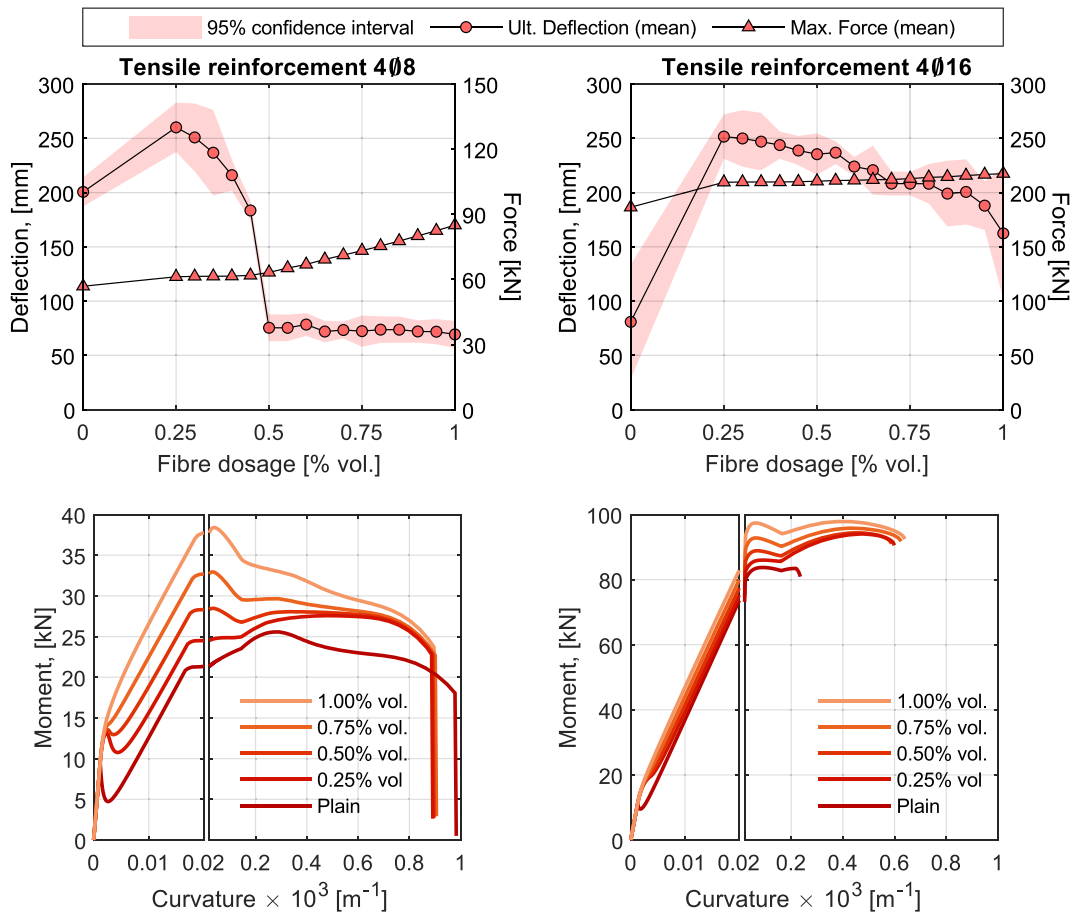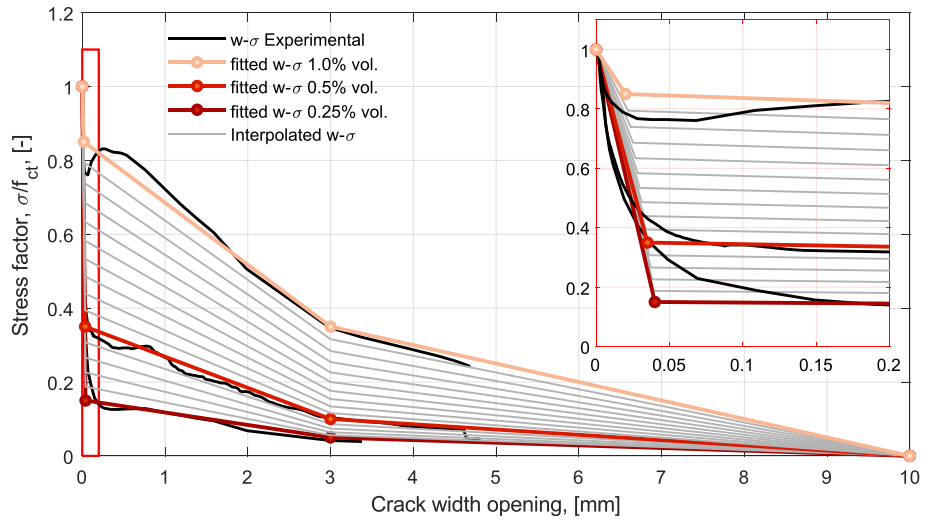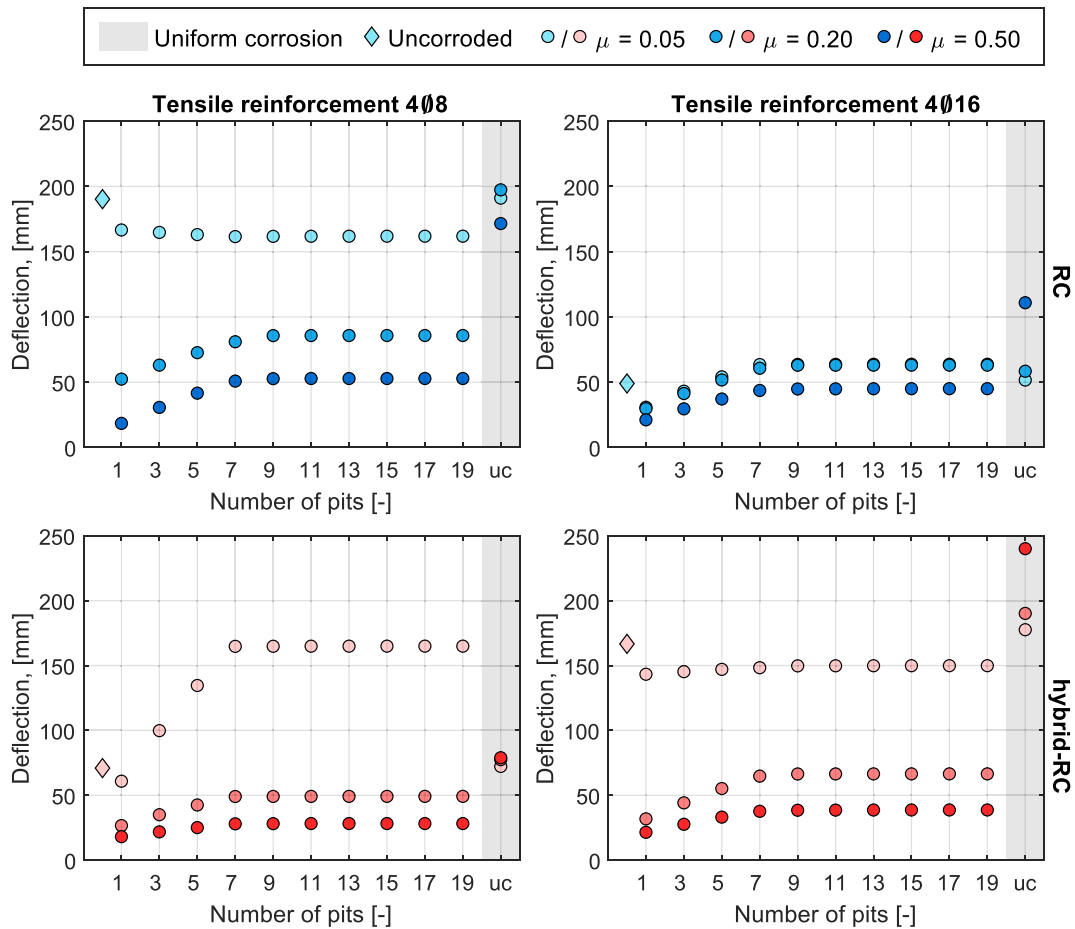

FIGURE 15 Numerical results of the ultimate deflection as a function of the fiber dosage (top) and moment curvature relationship at different fiber dosages (bottom) for hybrid-RC beams with two different reinforcement ratios.

increase is caused by the more ductile behavior of FRC in compression as described by the constitutive law proposed by Ruiz et al.[46] However, even though the mentioned constitutive law was calibrated using a large database including a wide range of fiber volumetric dosages spanning from 0.24% to 3.0%, it could still be questioned whether such a small fiber dosage can provide the predicted increased ductility.

An additional observation from Figure 15 is that the crack pattern and hence the variation of the hinge lengths, did not have any apparent effect on the maximum load. On the other hand, a certain variability can

FIGURE 16 Numerical results of the ultimate deflection as a function of the number corrosion pits along the beam for RC (top) and hybrid-RC (bottom) beams with two different reinforcement ratios.

be observed for the ultimate deflection, although no particular trend regarding the effect of fiber content or reinforcement ratio is obvious from the presented results.

5.3 | The effect of corrosion distribution for increasing corrosion levels

One of the main advantages of the proposed model is the possibility to easily include one or several localized corrosion pits at different locations in the beam. To that end, the effect of the corrosion distribution along the reinforcement on the deformation capacity of RC and hybrid-RC beams is investigated by progressively increasing the number of pits in the beams. The same beam geometry, material properties and loading configuration as in Section 5.1 were used. The analysis started by considering a single corrosion pit initially placed at the mid-hinge. Thereafter, the number of pits was progressively increased by including pitting in the two adjacent hinges. This was successively repeated until pitting was considered in all the 21 hinges. As in Section 5.1, it was

assumed that all bars in a hinge had the same corrosion level. Moreover, the same corrosion level was also considered in all hinges. However, three different corrosion level cases were investigated, namely 0.05, 0.2, and 0.5. Furthermore, a uniformly distributed corrosion case was also considered where the strain localization effect on the deformation capacity was not included. For the uniform corrosion case, the mechanical properties of an uncorroded steel bar were used but reducing the cross-sectional area of the tensile reinforcement in Equations (22) and (23).

Figure 16 summarizes the results of the effect of corrosion distribution in RC and hybrid-RC beams with low and high reinforcement ratios for three different corrosion levels. As expected, having one single corrosion pit in the most loaded section of the beam is always detrimental with regard to the deformation capacity compared to the uncorroded case. Likewise, increasing the corrosion level of the pits resulted in a generalized loss of ultimate deflection. However, increasing the number of pits had a positive effect on the ultimate deflection which in some cases led to a deformation capacity greater than

that of the uncorroded beam. The positive effect is, however, only observed up to seven pits, which corresponds to the number of hinges located in the constant moment region. This suggests that the effect of corrosion distribution on the deformation capacity cannot be uncoupled from the moment distribution in the beam. Finally, the uniformly distributed corrosion analyses predicted in general a deformation capacity similar or higher than that of the uncorroded beam. However, it should be noted that for the corrosion levels considered, there is a risk that the beam does not exhibit a typical bending failure when uniform corrosion is present. Therefore, further analyses should be performed to ensure that bending failure is the relevant failure mode.

6 | CONCLUSIONS

In the present paper, a modeling approach based on the nonlinear hinge model was developed to analyze the residual flexural response of hybrid-RC elements with localized pitting corrosion. The main findings of this work can be summarized as follows:

A new mechanical model was presented to describe the stress–strain relationship of steel reinforcement bars with localized pitting corrosion including nonlinear strain hardening and softening up to steel rupture. The model explicitly considers the reduction of deformation capacity due to strain localization in the pits.

The performance of the proposed modeling approach was evaluated in terms of its predictive capabilities using available experimental data in the form of force–deflection diagrams from RC and hybrid-RC beams with and without corrosion. The model showed a reasonably good agreement with the experiments. However, it was found that the model results were sensitive to the post-peak behavior of the concrete in compression controlled by the localization of concrete crushing and to a lesser degree also to the postcracking residual stress of FRC in tension governed by the stress-crack opening relationship.

From a parametric study carried out with the developed modeling approach, it was verified that the load capacity of both RC and hybrid-RC beams failing in bending decreased almost linearly when the corrosion level of a single pit in the most loaded section was gradually increased. The deformation capacity, on the other hand, was strongly dependent on the combination of reinforcement ratio and postcracking stress of the concrete for moderate corrosion levels up to 0.25. For local corrosion levels beyond 0.25, the ultimate deflection was governed by the deformation capacity of the corroded rebar.

Small fiber volumetric ratios (<0.4% vol.) were found to have a positive effect on the deformation capacity of beams with low reinforcement ratios whereas increasing the postcracking stress of concrete caused the peak moment to occur at a lower curvature compared to the RC case, leading to localization of rotation in a single section and the subsequent loss of deformation capacity.

The parametric study also revealed that having corrosion pits of a similar corrosion level in multiple sections may be beneficial with respect to the deformation capacity of the beam compared to having one single pit. However, including corrosion pits in sections with low moment demands had no impact on the flexural response of the beams.

NOMENCLATURE
Latin letters

$A_{i,\mathrm{corr}}$	average residual cross-sectional area of tensile reinforcement in a hinge
A_{pit}	minimum residual cross-sectional area at the pit of a corroded bar
$A_{\mathrm{s}}, A_{\mathrm{s}}'$	nominal reinforcement cross-sectional area (tension, compression)
a	crack height
b	beam width
$d_{\mathrm{s}}, d_{\mathrm{s}}'$	effective depth of reinforcement (tension, compression)
$E_{\mathrm{c}}, E_{\mathrm{s}}$	elastic modulus of concrete and steel
E_{sh_0}	strain-hardening modulus of steel reinforcement
F_y, F_p, F_u	force (yield, proof, ultimate)
F^k	applied force at kth loading step
f_{c}	concrete compressive strength
f_{ct}	concrete tensile strength
$f_y, f_{y,0}$	steel yield strength (general, uncorroded)
f_{p}	steel proof strength
$f_{\mathrm{u}}, f_{\mathrm{u},0}$	steel ultimate strength (general, uncorroded)
$f_{\mathrm{r},0}$	steel rupture strength (uncorroded)
h	beam height
h_i	ith hinge
K_{II}	bending stiffness at stabilized cracking stage
K_{unload}	unloading stiffness
ΔL	length increment
L	beam length
L_1	distance of load to support in four-point bending setup
l_{g}	gauge length
l_{p}	pit length
$M_{\mathrm{int}}, M_{\mathrm{ext}}$	bending moment (internal, external)
$M_i^k, M_{\mathrm{mid}}^k$	bending moment at the kth load step (ith hinge, mid-hinge)
$N_{\mathrm{int}}, N_{\mathrm{ext}}$	axial force (internal, external)

N_h number of hinges

n_{bars} number of tensile reinforcement bars

P   strain-hardening power exponent

s, s_i hinge length (general, ith hinge)

s_r average crack spacing

w, w_{CMOD} crack width, crack mouth opening displacement

w_i ith crack width opening in the stress-crack width relationship

y vertical coordinate with origin at the top of the cross-section

y_0 depth of the neutral axis

$x_{w,i}$ position of the beam's ith crack

Δx increment of length coordinate

Greek symbols

α_h strain-hardening fitting parameter

α_i ith stress to strength ratio in the stress-crack width relationship

δ_{max}^k maximum deflection at the kth load step

$\varepsilon_{c,0}$ concrete strain at peak stress (in compression)

$\varepsilon_s^{l_g}$ average steel strain over a gauge length l_g

$\varepsilon_y, \varepsilon_{y,0}$ steel yield strain (general, uncorroded)

$\varepsilon_{sh}, \varepsilon_{sh,0}$ steel strain at the onset of strain-hardening (general, uncorroded)

$\varepsilon_u, \varepsilon_{u,0}$ steel ultimate strain (general, uncorroded)

$\varepsilon_{r,0}$ steel rupture strain (general, uncorroded)

ε_t total strain

θ, θ^* rotation (general, crack planes)

ν_f volumetric fiber dosage

$\mu, \mu_{i,j}$ corrosion level at pit (general, at the jth bar of the ith hinge)

μ_{crit} critical corrosion level beyond which yielding localizes in a pit

$\mu_{i,mean}$ average corrosion level of tensile reinforcement at the ith hinge

$\mu_{i,max}$ maximum corrosion level of tensile reinforcement at the ith hinge

ρ_s steel reinforcement ratio

σ_c, σ_{ct} concrete stress (compression, tension)

σ_s, σ_s' steel stress (compression, tension)

χ_m average curvature

χ_i^k, χ_{mid}^k curvature at the kth load step (ith hinge, mid-hinge)

$\Delta \chi$ increment of curvature

Symbols

$\emptyset$ bar diameter

DATA AVAILABILITY STATEMENT

Data sharing is not applicable to this article as no new data were created or analyzed in this study.

ORCID

Carlos G. Berrocal https://orcid.org/0000-0003-4654-5498

E Chen https://orcid.org/0000-0002-9702-7757

Ingemar Löfgren https://orcid.org/0000-0002-8096-1375

Karin Lundgren https://orcid.org/0000-0002-4516-7440

REFERENCES

1. Fernandez I, Berrocal CG. Mechanical properties of 30 year-old naturally corroded steel reinforcing bars. Int J Concr Struct Mater. 2019;13(9) [under review].

2. Finozzi I, Saetta A, Budelmann H. Structural response of reinforcing bars affected by pitting corrosion: experimental evaluation. Construct Build Mater. 2018;192:478–88. https://doi.org/10.1016/j.conbuildmat.2018.10.088

3. Du YG, Clark LA, Chan AHC. Effect of corrosion on ductility of reinforcing bars. Mag Concr Res. 2005;57(7):407–19. https://doi.org/10.1680/macr.2005.57.7.407

4. Vandewalle L. Cracking behaviour of concrete beams reinforced with a combination of ordinary reinforcement and steel fibers. Mater Struct. 2000;33(3):164–70. https://doi.org/10.1007/BF02479410

5. Candido L, Micelli F, Vasanelli E, Aiello MA, Plizzari G. Cracking behaviour of FRC beams under long-term loading. 10th International Conference on Mechanics and Physics of Creep, Shrinkage, and Durability of Concrete and Concrete Structures September 21–23; 2015. p. 1147–56. https://doi.org/10.1061/9780784479346.137

6. Tiberti G, Minelli F, Plizzari G. Cracking behavior in reinforced concrete members with steel fibers: a comprehensive experimental study. Cem Concr Res. 2015;68:24–34. https://doi.org/10.1016/j.cemconres.2014.10.011

7. Abrishami HH, Mitchell D. Influence of steel fibers on tension stiffening. ACI Struct J. 1997;94(6):769–76.

8. Noghabai K. Behavior of tie elements of plain and fibrous concrete and varying cross sections. ACI Struct J. 2000;97(2):277–85. https://doi.org/10.14359/857

9. Bischoff PH. Tension stiffening and cracking of steel fiber-reinforced concrete. J Mater Civil Eng. 2003;15(2):174–82. https://doi.org/10.1061/(ASCE)0899-1561(2003)15:2(174)

10. Berrocal CG, Löfgren I, Lundgren K, Görander N, Halldén C. Characterisation of bending cracks in R/FRC using image analysis. Cem Concr Res. 2016;90:104–16. https://doi.org/10.1016/j.cemconres.2016.09.016

11. Berrocal CG, Löfgren I, Lundgren K, Tang L. Corrosion initiation in cracked fibre reinforced concrete: influence of crack width, fibre type and loading conditions. Corros Sci. 2015;98:128–39. https://doi.org/10.1016/j.corsci.2015.05.021

12. Sappakittipakorn M, Banthia N. Corrosion of rebar and role of fiber reinforced concrete. J Test Eval. 2012;40(1):103873. https://doi.org/10.1520/JTE103873

13. Berrocal CG, Fernandez I, Lundgren K, Löfgren I. Corrosion-induced cracking and bond behaviour of corroded reinforcement bars in SFRC. Compos Part B Eng. 2017;113:123–37. https://doi.org/10.1016/j.compositesb.2017.01.020

14. Wu K, Zheng H, Zhao J, Li H, Lin J. Experimental study on interfacial bond behavior and analysis of bond stress of steel and steel fiber reinforced concrete composite structure. Structure. 2021;30:156–65. https://doi.org/10.1016/j.istruc.2021.01.005

15. Blunt J, Jen G, Ostertag CP. Enhancing corrosion resistance of reinforced concrete structures with hybrid fiber reinforced concrete. Corros Sci. 2015;92:182–91. https://doi.org/10.1016/j.corsci.2014.12.003

16. Berrocal CG, Lundgren K, Löfgren I. Corrosion of steel bars embedded in fibre reinforced concrete under chloride attack: state of the art. Cem Concr Res. 2016;80:69–85. https://doi.org/10.1016/j.cemconres.2015.10.006

17. Marcos-Meson V, Michel A, Solgaard A, Fischer G, Edvardsen C, Skovhus TL. Corrosion resistance of steel fibre reinforced concrete—a literature review. Cem Concr Res. 2018;103:1–20. https://doi.org/10.1016/j.cemconres.2017.05.016

18. Berrocal CG, Löfgren I, Lundgren K. The effect of fibres on steel bar corrosion and flexural behaviour of corroded RC beams. Eng Struct. 2018;163:409–25. https://doi.org/10.1016/j.engstruct.2018.02.068

19. Chen E, Berrocal CG, Löfgren I, Lundgren K. Comparison of the service life, life-cycle costs and assessment of hybrid and traditional reinforced concrete through a case study of bridge edge beams in Sweden. Struct Infrastruct Eng. 2023;19(1):39–57. https://doi.org/10.1080/15732479.2021.1919720

20. Jnaid F, Aboutaha RS. Residual flexural strength of corroded reinforced concrete beams. Eng Struct. 2016;119:198–216. https://doi.org/10.1016/j.engstruct.2016.04.018

21. Lee HS, Noguchi T, Tomosawa F. The evaluation of flexural strength of RC beams damaged by rebar corrosion. In Lacasse MA, Vanier DJ. (Eds.), *Durability of building materials and components; Institute for Research in Construction*, Ottawa ON: National Research Council Canada; 1999. p. 321–30.

22. Lim S, Akiyama M, Frangopol DM. Assessment of the structural performance of corrosion-affected RC members based on experimental study and probabilistic modeling. Eng Struct. 2016;127:189–205. https://doi.org/10.1016/j.engstruct.2016.08.040

23. Habibi S, Ferche AC, Vecchio FJ. Modeling corrosion-damaged reinforced concrete members. ACI Struct J. 2022;119(1):169-182. https://doi.org/10.14359/51733011

24. Nasser H, Vrijdaghs R, van Steen C, Vandewalle L. Effect of corrosion damage on the tension-stiffening effect: a numerical investigation of the RC tension bar. 2nd CACRCS workshop capacity assessment of corroded reinforced concrete structures; organized by cte-eventi and fib. Online workshop; 2020. Available from: https://www.researchgate.net/publication/348494651

25. Haefliger S, Kaufmann W. Corroded tension chord model: load–deformation behavior of structures with locally corroded reinforcement. Struct Concr. 2022;23(1):104–20. https://doi.org/10.1002/suco.202100165

26. Berrocal CG, Fernandez I, Rempling R. The interplay between corrosion and cracks in reinforced concrete beams with non-uniform reinforcement corrosion. Mater Struct. 2022;55(4):120. https://doi.org/10.1617/s11527-022-01956-2

27. Chen E, Berrocal CG, Löfgren I, Lundgren K. Correlation between concrete cracks and corrosion characteristics of steel reinforcement in pre-cracked plain and fibre-reinforced concrete beams. Mater Struct. 2020;53(2). https://doi.org/10.1617/s11527-020-01466-z

28. Ulfkjær JP, Brincker R, Krenk S. Analytical model for complete moment-rotation curves of concrete bemas in bending. Depteratment of Building Technology and Structural Engineering, Aalborg University. Fracture and Dynamics; 1990;R9021(24). https://vbn.aau.dk/en/publications/analytical-model-for-complete-moment-rotation-curves-of-concrete–2.

29. Hillerborg A, Modéer M, Petersson P-E. Analysis of crack formation and crack growth in concrete by means of fracture mechanics and finite elements. Cem Concr Res. 1976;6(6):773–81. https://doi.org/10.1016/0008-8846(76)90007-7

30. Hillerborg A. Analysis of fracture by means of the fictitious crack model, particularly for fibre reinforced concrete. Int J Cem Compos. 1980;2(4):117–84.

31. Pedersen C, Mørk V, Stang H. New production processes, materials and calculation techniques for fiber reinforced concrete pipes. Lyngby, Denmark: Technical University of Denmark (DTU); 1997.

32. Casanova P, Rossi P. Analysis and design of steel fiber-reinforced concrete beams. ACI Struct J. 1997;94(5):595–602.

33. Olesen JF. Fictitious crack propagation in fiber-reinforced concrete beams. J Eng Mech. 2001;127(3):272–80. https://doi.org/10.1061/(ASCE)0733-9399(2001)127:3(272)

34. Olesen JF. Cracks in reinforced FRC beams subject to bending and axial load. *Fracture mechanics of concrete structures*; Netherlands: Swets & Zeitlinger; 2001. p. 1027–33.

35. Chen E, Berrocal CG, Fernandez I, Löfgren I, Lundgren K. Assessment of the mechanical behaviour of reinforcement bars with localised pitting corrosion by digital image correlation. Eng Struct. 2020;219:110936. https://doi.org/10.1016/j.engstruct.2020.110936

36. Rocha M, Brühwiler E, Nussbaumer A. Geometrical and material characterization of quenched and self-tempered steel reinforcement bars. J Mater Civil Eng. 2016;28(6). https://doi.org/10.1061/(ASCE)MT.1943-5533.0001355

37. Cairns J, Plizzari G, Du Y, Law DW, Franzoni C. Mechanical properties of corrosion-damaged reinforcement. ACI Mater J. 2005;4(2):256–264.

38. Andisheh K, Scott A, Palermo A. Modeling the influence of pitting corrosion on the mechanical properties of steel reinforcement. Mater Corros. 2016;67(11):1220–34. https://doi.org/10.1002/maco.201508795

39. Franceschini L, Belletti B, Tondolo F, Sanchez Montero J. A simplified stress–strain relationship for the mechanical behavior of corroded prestressing strands: the SCPS-model. Struct Concr. 2022;24(1):189–210. https://doi.org/10.1002/suco.202200170

40. ISO EN 6892-1:2009. Metallic materials—tensile testing—Part 1: method of test at room temperature. 2009.

41. Mander JB. Seismic design of bridge piers. Christchurch, New Zealand: University of Canterbury; 1983.

42. EN 1992-1-1 Eurocode 2. EN 1992-1-1 Eurocode 2: design of concrete structures—part 1-1: general rules and rules for buildings. Brussels, Belgium: European Committee for Standardization; 2004.

43. Löfgren I. Analysis of flexural behaviour of reinforced FRC members. Nordic Miniseminar: Desgin rules for steel fibre reinforced concrete structures; Oslo: The Nordic Concrete Federatoin; 2003 Available from: https://www.researchgate.net/publication/257944070

44. RILEM TC 162-TDF. Recommendations of RILEM TC 162-TDF: test and design methods for steel fibre reinforced concrete Uniaxial tension test for steel fibre reinforced concrete. Mater Struct. 2005;34(235):3–6. https://doi.org/10.1617/13628

45. Thorenfeldt E, Tomaszewicz A, Jensen JJ. Mechanical properties of high-strength concrete and applications in design. Symposium utilization of high-strength concrete, Stavanger, Norway, 15–18 June 1987; Publisher: Tapir, Trondheim, pp. 149–159.

46. Ruiz G, de la Rosa Á, Wolf S, Poveda E. Model for the compressive stress–strain relationship of steel fiber-reinforced concrete for non-linear structural analysis. Hormigón Acero. 2018;69 (S1):75–80. https://doi.org/10.1016/j.hya.2018.10.001

47. Hanjari KZ, Kettil P, Lundgren K. Modelling the structural behaviour of frost-damaged reinforced concrete structures. Struct Infrastruct Eng. 2013;9(5):416–31. https://doi.org/10.1080/15732479.2011.552916

48. Barros JAO, Taheri M, Salehian H. A model to simulate the moment–rotation and crack width of FRC members reinforced with longitudinal bars. Eng Struct. 2015;100:43–56. https://doi.org/10.1016/j.engstruct.2015.05.036

49. Schupack M. Durability of SFRC exposed to severe environements. US-Sweden joint seminar (NSF-STU); Stockholm: Swedish Cement and Concrete Research Institute; 1985. p. 479–96.

50. Mangat PS, Gurusamy K. Corrosion resistance of steel fibres in concrete under marine exposure. Cem Concr Res. 1988;18:44–54.

51. Granju J-L, Balouch SU. Corrosion of steel fibre reinforced concrete from the cracks. Cem Concr Res. 2005;35(3):572–7. https://doi.org/10.1016/j.cemconres.2004.06.032

52. Jansson A, Löfgren I, Gylltoft K. Flexural behaviour of members with a combination of steel fibres and conventional reinforcement. Nordic Concr Res. 2010;2(2010):155–77. Available from: https://www.researchgate.net/publication/257924660

53. Löfgren I, Stang H, Olesen JF. The WST method, a fracture mechanics test method for FRC. Mater Struct. 2007;41(1):197–211. https://doi.org/10.1617/s11527-007-9231-3

54. Jepsen MS, Damkilde L, Lövgren I, Berrocal C. Adaptive inverse analysis (AIA) applied and verified on various fiber reinforced concrete composites. Mater Struct. 2018;51(3). https://doi.org/10.1617/s11527-018-1177-0

55. Markić T, Amin A, Kaufmann W, Pfyl T. Strength and deformation capacity of tension and flexural RC members containing steel fibers. J Struct Eng. 2020;146(5). https://doi.org/10.1061/(ASCE)ST.1943-541X.0002614

AUTHOR BIOGRAPHIES

Carlos G. Berrocal, Ph.D., Researcher, Structural Engineering Division, Chalmers University of Technology/Thomas Concrete Group C-lab, Gothenburg, Sweden; carlos.gil@chalmers.se

E. Chen, Associate Professor, School of Civil and Hydraulic Engineering, Huazhong University of Science and Technology, Wuhan, China.

Ingemar Löfgren, Ph.D., Ajunct Professor, Structural Engineering Division, Chalmers University of Technology/Thomas Concrete Group C-lab, Gothenburg, Sweden.

Karin Lundgren, Professor, Structural Engineering Division, Chalmers University of Technology, Gothenburg, Sweden.